2014•2015
FACULTEIT INDUSTRIËLE INGENIEURSWETENSCHAPPEN
master in de industriële wetenschappen: energie

Masterproef

Lock-in infrared thermography as non-destructive test for material characterization

Promotor :
Prof. dr. ir. Michael DAENEN
Prof. dr. Ward DE CEUNINCK

Promotor :
prof. dr. WARD DECEUNINCK

Len Bussé , Jorne Carolus
Scriptie ingediend tot het behalen van de graad van master in de industriële wetenschappen: energie

Gezamenlijke opleiding Universiteit Hasselt en KU Leuven

KU LEUVEN | universiteit hasselt

2014•2015
Faculteit Industriële ingenieurswetenschappen
master in de industriële wetenschappen: energie

Masterproef

Lock-in infrared thermography as non-destructive test for material characterization

Promotor :
Prof. dr. ir. Michael DAENEN
Prof. dr. Ward DE CEUNINCK

Promotor :
prof. dr. WARD DECEUNINCK

Len Bussé , Jorne Carolus
Scriptie ingediend tot het behalen van de graad van master in de industriële wetenschappen: energie

universiteit hasselt | KU LEUVEN

Acknowledgements

This master's thesis is the final element of our education to Master of Science in Engineering with a major in Energy at University Hasselt and KU Leuven. The realization of this master's thesis was a challenging but interesting experience. Without the participation and assistance of others, this work would not have been possible. Therefore, we would like to thank everyone who contributed to the different aspects of this master's thesis.

In particular, we would like to express our deepest gratitude to our promoter prof. dr. ir. Michaël Daenen and co-promoter prof. dr. Ward De Ceuninck. Lots of freedom was given to us, while providing us with the direction we needed. They always helped us when we encountered a problem with additional information, excellent guidance and sufficient patience.

Also thanks to our co-workers at the Research Institute for Materials, in particular ing. Jan Mertens and mr. Lieven De Winter. Their critical approach and observations combined with their enthusiasm constituted an extra stimulus to bring this thesis to a successful end. We could always rely on them when we encountered a problem of any kind.

We would also like to thank our family, friends and everyone who has helped us in one way or another. In particular, thanks to our parents for their support throughout our academic career.

Len Bussé & Jorne Carolus
June 2015

Table of Contents

Acknowledgements i

List of Tables v

List of Figures viii

List of Abbreviations ix

List of Symbols xi

Abstract xiii

Samenvatting xv

Chapter 1 Introduction 1
- 1.1 Problem Statement . . . 1
- 1.2 Objectives . . . 2
- 1.3 Methodology . . . 2
- 1.4 Outline of the Dissertation . . . 2

Chapter 2 Literature Review 5
- 2.1 Infrared Radiation . . . 5
  - 2.1.1 Electromagnetic Waves . . . 5
  - 2.1.2 Infrared and the Electromagnetic Spectrum . . . 6
  - 2.1.3 Infrared Radiation Principles . . . 6
  - 2.1.4 Emissivity . . . 8
  - 2.1.5 Atmospheric Infrared Window . . . 9
- 2.2 Infrared Thermography . . . 11
  - 2.2.1 Infrared Camera . . . 11
  - 2.2.2 Image Formation . . . 11
  - 2.2.3 Detectors . . . 14
  - 2.2.4 Digitization . . . 18
  - 2.2.5 Field of View . . . 19
  - 2.2.6 Temperature Measurements . . . 20
  - 2.2.7 Advantages and Disadvantages . . . 21
- 2.3 Lock-In Infrared Thermography . . . 22
  - 2.3.1 Non-Destructive Testing . . . 22
  - 2.3.2 Infrared Thermography in Non-Destructive Testing . . . 22
  - 2.3.3 Lock-In Infrared Thermography as Non-Destructive Test . . . 23
  - 2.3.4 Advantages and Disadvantages . . . 27

Chapter 3 Materials and Methods **29**
3.1 Hardware . . . 29
3.1.1 Infrared Camera . . . 29
3.1.2 Excitation Source . . . 30
3.1.3 Data Analyzer . . . 33
3.2 Software . . . 34
3.2.1 LabVIEW . . . 34
3.2.2 ImageJ . . . 34

Chapter 4 Design Results **37**
4.1 Hardware . . . 37
4.1.1 Power Amplifier . . . 37
4.2 Software . . . 40
4.2.1 Lock-In Infrared Thermography in LabVIEW . . . 40

Chapter 5 Defect Detection using Lock-In Infrared Thermography **45**
5.1 Photovoltaic Cell . . . 45
5.1.1 Introduction . . . 45
5.1.2 Experimental Setup . . . 45
5.1.3 Test Results . . . 46
5.1.4 Conclusion . . . 46
5.2 Meander Resistor . . . 47
5.2.1 Introduction . . . 47
5.2.2 Experimental Setup . . . 47
5.2.3 Test Results . . . 48
5.2.4 Conclusion . . . 48
5.3 Carbon Fiber Reinforced Polymer Substrate . . . 49
5.3.1 Introduction . . . 49
5.3.2 Experimental Setup . . . 49
5.3.3 Test Results without Defect . . . 50
5.3.4 Test Results with Defect . . . 51
5.3.5 Conclusion . . . 51

Chapter 6 Conclusions **53**

Bibliography **57**

List of Tables

Table 2.1 The Composition of the Earth's Dry Atmosphere 9
Table 2.2 A commonly Used Subdivision Scheme for the Infrared Spectrum 10
Table 2.3 The Useful Portions of the Infrared Spectrum for Infrared Thermography 10
Table 2.4 The Most Commonly Used Infrared Detectors 18

Table 3.1 The Specifications of the FLIR A5sc and the FLIR E40 30
Table 3.2 The Specifications of the Dell LATITUDE E5440 33

List of Figures

Figure 2.1 An Electromagnetic Wave 5
Figure 2.2 The Electromagnetic Spectrum 6
Figure 2.3 The Visual Representation of Planck's Law 7
Figure 2.4 The Emissivity of a Black Body, a Grey Body and a Selective Radiator . . 8
Figure 2.5 The Atmospheric Infrared Window with the Absorbing Molecules 9
Figure 2.6 The Main Components of an Infrared Camera 11
Figure 2.7 The Scanning and Staring System for Image Formation 11
Figure 2.8 The Block Diagram of a Read Out Integrated Circuit 12
Figure 2.9 A Comparison of Different Array Sizes for a 1 Megapixel Image 13
Figure 2.10 The Fill Factor of a Focal Plane Array 13
Figure 2.11 The Infrared Camera's Offset Compensation 13
Figure 2.12 The Infrared Camera's Slope Correction 14
Figure 2.13 The Infrared Camera's Non-Uniformity Correction 14
Figure 2.14 A Microbolometer Element 15
Figure 2.15 The Signal Generation and Readout in a Bolometer Camera 16
Figure 2.16 The Intrinsic Photoelectric Effect 16
Figure 2.17 The Signal Generation and Readout in a Quantum Detector Camera . . . 17
Figure 2.18 The Relative Response Curves for Different Detector Types 17
Figure 2.19 A Three-Dimensional Function of an Object's Emitted Infrared 18
Figure 2.20 The Field of View 19
Figure 2.21 The Total Incident Radiation on the Infrared Camera Lens 20
Figure 2.22 The Fundamental Setup to Perform Passive Infrared Thermography . . . 22
Figure 2.23 The Fundamental Setup to Perform Active Infrared Thermography 23
Figure 2.24 The Lock-In Principle (a Discrete Fourier Transform) 25
Figure 2.25 The Discrete Fourier Transform for a Matching Signal 26
Figure 2.26 The Discrete Fourier Transform for a Matching Signal 26

Figure 3.1 The FLIR A5sc and FLIR E40 Infrared Cameras 29
Figure 3.2 The Keithley 3390 Arbitrary Waveform/Function Generator 30
Figure 3.3 The LED Engin LZ9-00CW00 Power LED 31
Figure 3.4 The Relative Spectral Power of the Power LED 31
Figure 3.5 The Forward Current in Function of the Forward Voltage of the Power LED 31
Figure 3.6 The Emitted Radiation Power of the Power LED 32
Figure 3.7 The Total Harmonic Distortion of the Power LED 32
Figure 3.8 The LabVIEW Front Panel View with the Controls Palette 35
Figure 3.9 The LabVIEW Block Diagram View with the Functions Palette 35

Figure 4.1 The Custom-Made Power Amplifier 37
Figure 4.2 The Wiring Diagram of the Power Amplifier 38
Figure 4.3 The Output Signal of the Power Amplifier 39
Figure 4.4 The Total Harmonic Distortion of the Power Amplifier 39
Figure 4.5 The User Interface of the Lock-In Infrared Thermography Main Program 40

Figure 4.6 The User Interface of the Setup Function Generator Subprogram 41
Figure 4.7 The User Interface of the Capture Data Subprogram 41
Figure 4.8 The User Interface of the Process Data Subprogram - Continuous Averaging 42
Figure 4.9 The User Interface of the Process Data Subprogram - Moving Averaging . 43

Figure 5.1 The Setup to Test a PV Cell with Lock-In IR Thermography 45
Figure 5.2 An Element of the IR Image Stream of the PV Cell 46
Figure 5.3 The Modulus Image of the PV Cell 46
Figure 5.4 The Phase Image of the PV Cell 46
Figure 5.5 The Setup to Test a Meander Resistor with Lock-In IR Thermography . . 47
Figure 5.6 An Element of the IR Image Stream of the Meander Resistor 48
Figure 5.7 The Modulus Image of the Meander Resistor 48
Figure 5.8 The Phase Image of the Meander Resistor 48
Figure 5.9 The Setup to Test a CFRP Substrate with Lock-In IR Thermography . . 49
Figure 5.10 An Element of the IR Image Stream of the CFRP Substrate without Defect 50
Figure 5.11 The Modulus Image of the CFRP Substrate without Defect 50
Figure 5.12 The Phase Image of the CFRP Substrate without Defect 50
Figure 5.13 An Element of the IR Image Stream of the CFRP Substrate with Defect . 51
Figure 5.14 The Modulus Image of the CFRP Substrate with Defect 51
Figure 5.15 The Phase Image of the CFRP Substrate with Defect 51

List of Abbreviations

CPU	Central Processing Unit
CFRP	Carbon Fiber-Reinforced Polymer
DDR	Double Date Rate
DFT	Discrete Fourier Transformation
EM	ElectroMagnetic
FIR	Far-Infrared
FOV	Field of View
FPA	Focal Plane Array
HFOV	Horizontal Field of View
IFOV	Instantaneous Field of View
IMEC	Interuniversity MicroElectronics Centre
INI	Initializing
IMO	Institute for Material Research
IMOMEC	Institute for Material Research in MicroElectronics
IR	Infrared Radiation
LCD	Liquid Crystal Display
LED	Light Emitting Diode
LWIR	Long-Wavelength Infrared
MCT	Mercury Cadmium Telluride
MWIR	Mid-Wavelength Infrared
NDT	Non-Destructive Testing
NETD	Noise Equivalent Temperature Difference
NI	National Instruments
NIR	Near-Infrared
NUC	Non-Uniformity Correction
PNG	Portable Network Graphics
PV	PhotoVoltaic
QWIP	Quantum Well Infrared Photodetector
RAM	Random-Access Memory
ROIC	Readout Integrated Circuit
SNR	Signal to Noise Ratio
SWIR	Short-Wavelength Infrared
THD	Total Harmonic Distortion
VFOV	Vertical Field of View
VI	Virtual Instrument

List of Symbols

A	Amplitude
α	Absorption Factor
b	Focal Plane Array Width/Length
$\overline{\beta R}$	Average Temperature Coefficient
c	Speed of Light
c_p	Specific Heat Capacity.
C_{th}	Heat Capacity.
d	Minimum Object Size
D	Object Distance
E	Quantum Energy
ϵ	Emissivity
f	Frequency
G_{th}	Heat Conductance
h	Planck's Constant
I	Current
k	Wavenumber
κ	Thermal Conductivity
l	Focal Length of the Camera
λ	Wavelength
M	Radiant Exitance
n	Number of Evaluated Frames Each Lock-In Period
N	Total Number of Evaluated Frames
P	Excitation Power
ϕ	Phase
Φ_0	Radiation Power
R	Resistance
ρ	Reflection Factor
ϱ	Mass Density
σ	Stefan-Boltzmann's Constant
ς	Thermal Diffusivity
t	Time
T	Absolute Temperature
$\boldsymbol{\tau}$	Transmission Factor
τ	Time Constant
U	Voltage
μ	Thermal Diffusion Length
ω	Angular Velocity
x	Observed Length
z	Penetration Depth
ζ	Amplification Factor

Abstract

The Research Institute for Materials, located at the university campus in Diepenbeek, comprises a research group, imo-imomec, committed to the development and characterization of new material systems. Material characterization can be done by means of destructive or non-destructive testing methods. However, the destructive testing methods are time consuming and economically inefficient since the test specimens are damaged during the process. The main objective of this master's thesis is to realize a demo setup to perform lock-in infrared thermography, a non-destructive testing method for material characterization.

The development of the demo setup comprised two parts. First, the hardware is compiled and consists of three major parts, i.e. the infrared camera, the excitation source and the data analyzer. Some of the hardware components, such as the power amplifier, are built for this specific application. Second, the software, which captures and processes the data images, was realized using LabVIEW. Algorithms for both continuous and moving averaging are included.

Lock-in infrared thermography is relatively fast and economically more efficient compared to destructive testing methods. Test results show that minor defects that are not visible to the naked eye, such as inhomogeneities, delaminations and internal fractures can be shown using this demo setup for lock-in infrared thermography.

Samenvatting

Het Onderzoeksinstituut voor Materialen, gelegen op de universitaire campus te Diepenbeek, omvat een onderzoeksgroep, imo-imomec, die zich voornamelijk inzet voor de ontwikkeling en karakterisering van nieuwe materiaalsystemen. Materiaalkarakterisering kan gebeuren met behulp van zowel destructive als niet-destructieve testmethoden. De destructive testmethode is echter tijdrovend en economisch inefficiënt aangezien de geteste materialen beschadigd worden tijdens het proces. Het hoofddoel van deze masterthesis is de realisatie van een demo-opstelling om lock-in infrarood thermografie, een niet-destructieve testmethode voor materiaalkarakterisering, te realiseren.

De ontwikkeling van de demo-opstelling bestond uit twee delen. Ten eerste is de hardware opstelling samengesteld. De hardware bestaat uit drie grote elementen, namelijk de excitatie bron, de infraroodcamera en de gegevensverwerker. Enkele hardwarecomponenten, zoals de vermogensversterker, zijn voor deze specifieke toepassing gebouwd. Ten tweede is de software die de data vastlegt en verwerkt gerealiseerd met behulp van LabVIEW. Algoritmes voor zowel continue als lopende middeling zijn inbegrepen.

Lock-in infrarood thermografie is relatief snel en economisch efficiënter in vergelijking met destructieve testmethoden. Testresultaten tonen aan dat kleine beschadigingen die niet zichtbaar zijn voor het blote oog, zoals inhomogeniteiten, delaminaties en interne breuken, aan te tonen zijn met behulp van deze demo-opstelling voor lock-in infrarood thermografie.

Chapter 1

Introduction

During the Master program in Engineering with a major in Energy at University Hasselt and KU Leuven, we had the opportunity to realize our master's thesis at the Research Institute for Materials (IMO), located in Diepenbeek (province of Limburg, Flanders, Belgium). The main goal was to realize a demo setup to perform non-destructive tests for material characterization.

The core competence of IMO is the development and characterization of new material systems with potential use in microelectronics, bioelectronics, energy and nanotechnology. In this core competence field, both fundamental and applied research programs are carried out.

A close cooperation is constituted between IMO and the Interuniversity MicroElectronics Centre (imec), located in Louvain (province of Flemisch Brabant, Flanders, Belgium). The local division Institute for Materials Research in MicroElectronics (IMOMEC) is housed within the premises of IMO. The major part of fundamental research in the core competence field is performed by IMO, while the majority of applied research programs is performed by IMOMEC in collaboration with several industrial partners.

Approximately 110 people are working at IMO-IMOMEC as a member of a highly interdisciplinary group of researchers (chemists, physicists, engineers, etc.). About 70 % of research funding at IMO-IMOMEC comes from applied research projects, mainly in collaboration with various industrial partners. The other 30 % is provided by the Flemish government and the university. [1]

1.1 Problem Statement

In one of the research fields at IMO, the research group 'energy systems engineering', led by prof. dr. ir. Michaël Daenen, is investigating the reliability of various energy systems such as photovoltaic cells, batteries, etc. For this purpose physical properties of multilayer materials are examined. Due to the manufacturing process, transportation or normal use, there is a chance that these multilayer materials can incur defects. These defects include inhomogeneities, delaminations and internal fractures, which are not visible to the naked eye. Additionally, internal contamination can result in failure of different materials, such as a p-n junction of a photovoltaic cell. Therefore, they can have a negative influence on the material properties without being noticed.

In order to display the above mentioned defects, samples are randomly selected and subjected to destructive tests. However, this is time consuming and expensive, especially since the tested specimens are damaged and not usable afterwards. Non-destructive testing methods can possibly alleviate this problem. Lock-in infrared thermography should be tested and evaluated to verify whether this technique can be useful as a non-destructive testing method.

1.2 Objectives

As a consequence of the above mentioned problems concerning the destructive testing ways, industries are put under economic pressure to develop and use a quicker and cheaper way to submit specimens to material characterization tests.

Specifically, the main purpose of this master's thesis is the development of a demo setup to perform non-destructive tests that complies with the above mentioned requirements. This project will focus on lock-in infrared thermography, a versatile tool for material and device characterization. The development includes both the hardware and the software part of the demo setup.

1.3 Methodology

First, a literature study was performed to obtain more knowledge on lock-in infrared thermography as a non-destructive testing method for material characterization. The acquired knowlegde is described in the literature review. Furthermore, the necessary hardware and software to perform the lock-in infrared thermography experiments is described.

Second, a demo setup sufficiently representing the daily practice was realized. Based on the acquired knowledge, each hardware and software item was selected to develop a demo setup according to the above mentioned requirements. The hardware setup consists of an infrared camera, an excitation source and a data analyzer. As for the software, LabVIEW and ImageJ were used.

Third, measurements on several real samples were performed. The measurements were conducted with two different excitation methods, i.e. electrical and optical excitation. The different excitation methods provided different material characteristics.

Fourth, the realized demo setup was optimized to obtain the most accurate test results possible. After optimizing the demo setup, new tests were performed and the results were compared with the previous results. Afterwards, a full automation of the software was carried out.

Fifth and final, a detailed report was written. This report contains the literature study, the materials and methods, the design results, the defect detection tests and the conclusions.

1.4 Outline of the Dissertation

The outline of this master's thesis is organized as follows.

In Chapter 2, the literature review is discussed with the three most important notions in order to comprehend the fundamentals of lock-in infrared thermography, i.e. infrared (Section 2.1), infrared thermography (Section 2.2) and lock-in infrared thermography (Section 2.3).

In Chapter 3, the materials and methods necessary to accomplish the demo setup are presented. Both the hardware (Section 3.1) and the software (Section 3.2) are discussed in detail. The hardware consists of an infrared camera, an excitation source and a data analyzer. The software used for the processing of the lock-in algorithm is LabVIEW. The software used for analysis of the test results is ImageJ.

In Chapter 4, the design results of the demo setup to perform lock-in infrared thermography are presented. This section is composed of a hardware part (Section 4.1) and a software part (Section 4.2). In the hardware part, calculation of the custom-made power amplifier is explained

in detail. In the software part, a manual to use the custom-made Lock-In Infrared Thermography program with its extensions is proposed.

In Chapter 5, three defect detection tests are discussed. The first defect detection test is conducted by an electrical excitation on a photovoltaic cell (Section 5.1). The second defect detection test is conducted by an electrical excitation on a meander resistor (Section 5.2). The third defect detection test is conducted by an optical excitation on a carbon fiber-reinforced polymer substrate (Section 5.3). The camera used during the three defect detection tests was the FLIR E40 infrared camera.

In Chapter 6, the conclusions and suggestions for future work are presented.

Chapter 2

Literature Review

2.1 Infrared Radiation

2.1.1 Electromagnetic Waves

Infrared radiation (IR) can be described as electromagnetic (EM) waves, together with radio waves, microwaves, visible light, ultraviolet radiation, X-rays and gamma rays. An EM wave is a transverse sinusoidal wave, which can propagate in a vacuum. The general equation of a sinusoidal wave is as follows:

$$y(x,t) = A * Sin(kx - \omega t + \phi) \tag{2.1}$$

Where A is the amplitude, k is the wavenumber ($k = \frac{2*\pi}{\lambda}$), ω is the angular velocity ($\omega = 2*\pi*f$) and ϕ is the phase.

Both frequency (f) and wavelength (λ) are connected via the speed of propagation (c) of the EM wave, which is $299,792,458\ \frac{m}{s}$, by following equation:

$$c = f * \lambda \tag{2.2}$$

As the name suggests, an EM wave consists of an electric field and a magnetic induction field. The electric field and the magnetic induction field are perpendicular to each other and to the direction of propagation. This principle is shown in Figure 2.1, where the wave propagates according to the z-axis. [2,3]

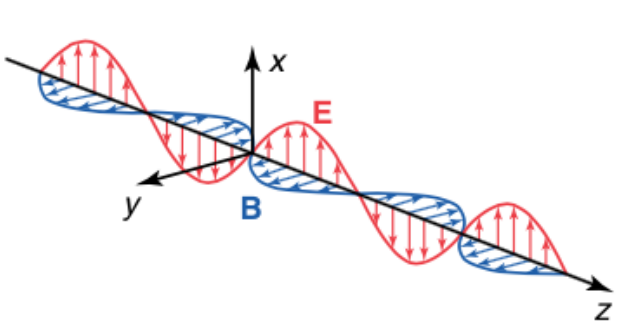

Figure 2.1: A representation of an EM wave, which propagates according to the z-axis. [2]

2.1.2 Infrared and the Electromagnetic Spectrum

As mentioned in Section 2.1.1, IR is an EM wave, which extends from the red edge of the visible spectrum at a wavelength of 700 nm (a frequency of 430 THz) to the microwave portion at a wavelength of 1 mm (a frequency of 300 GHz). This is shown in Figure 2.2. All matter at a temperature above absolute zero (0 K) emits IR and the amount of radiation increases with the temperature. Although IR cannot be seen with the naked eye, it can be sensed as heat. Short wavelength radiation, such as gamma rays, X-rays and ultraviolet, carries the highest energy and can be very dangerous. Longer wavelength radiation, such as microwaves and IR, is of lower energy and is usually less harmful.

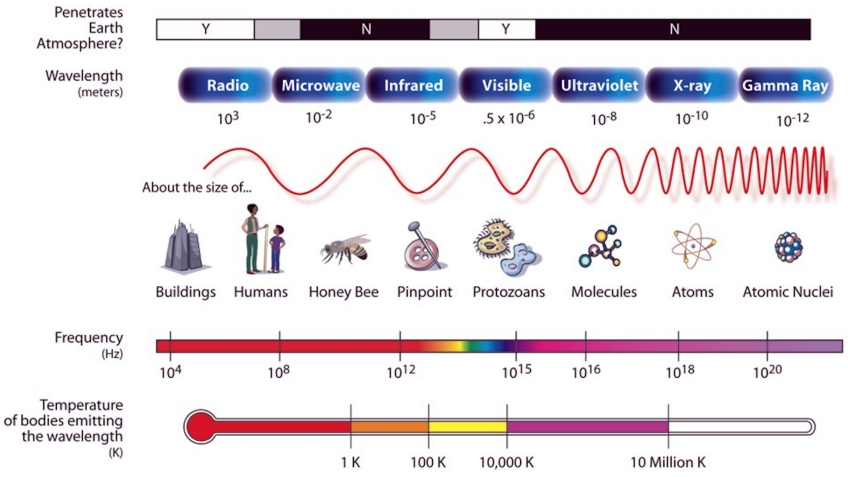

Figure 2.2: The electromagnetic spectrum and its properties for varying wavelengths. [4]

The discovery of IR is ascribed to the British astronomer Sir William Herschel and dates from the year 1800. Herschel measured the difference in temperature between the colors in the visible spectrum using a prism to refract the light coming from the sun. He discovered an increase in temperature from blue to red, but more important, he noticed an even warmer temperature just beyond the red end of the visible spectrum. Herschel called these invisible rays 'calorific rays'. The term 'infrared' did not appear until late in the 19th century. [4–10]

2.1.3 Infrared Radiation Principles

The intensity of the emitted radiation is dependent on both the temperature and the radiated wavelength. The emitted radiation is located completely within IR wavelengths if the object has a temperature less than 480 degrees Celsius. Depending on the object's properties, the incident radiation will be partially absorbed (α), reflected (ρ) or transmitted ($\boldsymbol{\tau}$). From this, the total radiation law can be derived and can be stated with the following equation:

$$M = \alpha M + \rho M + \boldsymbol{\tau} M \tag{2.3}$$

Where M is the radiant exitance expressed in $[\frac{W}{sr*m^2}]$. Equation 2.3 can be simplified to:

$$1 = \alpha + \rho + \boldsymbol{\tau} \tag{2.4}$$

For instance, if $\rho = 0$, $\boldsymbol{\tau} = 0$ and $\alpha = 1$, there is no reflected nor transmitted radiation and 100 % of incident radiation is absorbed. A matter that absorbs all incident radiation is called a perfect black body. In reality, there are no objects that are perfect absorbers, reflectors or transmitters. However, because it is the foundation for relating IR to an object's temperature, the term of a perfect black body is very important.

The radiated power per unit area of a perfect black body as a function of the wavelength can be described mathematically by Planck's law:

$$M_\lambda(T) = \frac{2\pi hc^2}{\lambda^5}(e^{\frac{hc}{\lambda\sigma T}} - 1)^{-1} \tag{2.5}$$

Where $M_\lambda(T)$ is expressed in $[\frac{W}{sr*m^3}]$, h is Planck's constant (6.626 069 57 x 10^{-34} J s), σ is Stefan-Boltzmann's constant (5.670373 x 10^{-8} kg s^{-3} K^{-4}) and T is the absolute temperature.

With regards to Equation 2.2 (Section 2.1.1), Planck's law for a black body can also be described as a function of the frequency:

$$M_f(T) = \frac{2\pi hf^3}{c^2}(e^{\frac{hf}{\sigma T}} - 1)^{-1} \tag{2.6}$$

Where $M_f(T)$ is expressed in $[\frac{W}{sr*m^2*Hz}]$. Nevertheless, a black body's radiative properties are usually displayed as a series of curves, as shown in Figure 2.3. These curves show the spectral radiant emittance of the black body. As mentioned in Section 2.1.2, the intensity of the emitted radiation will increase with increasing temperature. However, each curve has a maximum value at a certain wavelength, which can be calculated from Wien's displacement law:

$$\lambda_{max} = \frac{2898}{T} \tag{2.7}$$

Where λ_{max} is the wavelength at the maximum intensity, expressed in $[\mu m]$.

The total radiated power per unit area of a perfect black body can be calculated by integrating Planck's law (Equation 2.5) over wavelength/frequency. This is expressed by a formula known as Stefan-Boltzmann's law:

$$M = \sigma T^4 \tag{2.8}$$

[2, 5, 11–14]

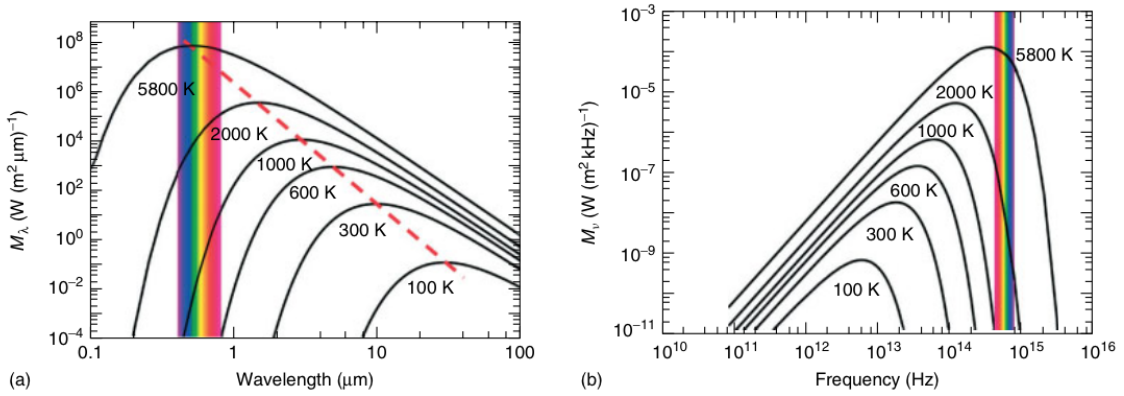

Figure 2.3: a) The black body radiation according to Planck's law in function of the wavelength. b) The black body radiation according to Planck's law in function of the frequency. [2]

2.1.4 Emissivity

The radiative properties of an object is usually represented as a perfect black body where α = emissivity (ε) = 1. As mentioned in Section 2.1.3, in reality there is no such thing as a black body. In practice, the value of the ε can be determined by the following equation:

$$\varepsilon = \frac{M_e}{M_e^\circ} \tag{2.9}$$

Where M_e is the radiant exitance of a real surface and M_e° the radiant exitance of a black body at the same temperature as the real surface. Therefore, the better the radiative properties of the real surface, the better it will approach the black body with an ε of 1.

For practical IR thermography, it is inconvenient to work with the definition of emissivity as shown in Equation 2.9. Therefore, a different approach to estimate the emissivity is needed. Kirchhoff's law states that the amount of radiation absorbed by any object is equal to the amount of radiation that is emitted by this object:

$$\varepsilon = \alpha \tag{2.10}$$

Substituting Equation 2.10 in Equation 2.4 (Section 2.1.3) estimates the emissivity, which for an opaque body ($\boldsymbol{\tau} = 0$) can be simplified to:

$$\varepsilon = 1 - \rho \tag{2.11}$$

This means that an estimation of emissivity is known when the value of reflectivity is known, which comes in handy for IR thermography.

An object of which the emissivity is independent of the wavelength is called a grey body. For a grey body, Stefan-Boltzmann's law is as follows:

$$M_e = \varepsilon \sigma T^4 \tag{2.12}$$

Nevertheless, black bodies and grey bodies do not occur in reality because the emissivity depends, among others, on the wavelength. Since thermography occurs in specific regions of the EM spectrum, it is often possible to treat an object as a grey body. An object with an emissivity that varies strongly with the wavelength is called a selective radiator. The emissivity coefficients in function of the wavelength of a black body, a grey body and a selective radiator are represented in Figure 2.4. [2, 5, 13, 14]

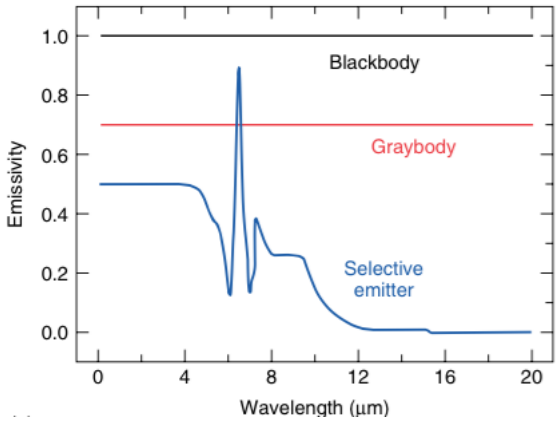

Figure 2.4: A representation of the emissivity coefficients in function of the wavelength of a black body, a grey body and a selective radiator. [2]

2.1.5 Atmospheric Infrared Window

The Earth's dry atmosphere is composed of different gases, of which the most important are shown in Table 2.1. Note that this is the composition of the dry atmosphere without any water vapor ($H_2O_{(g)}$). The amount of $H_2O_{(g)}$ in the Earth's atmosphere varies strongly depending on the area and can take values between 0.0001 % and 5 % in volume.

Table 2.1: The major constituents of Earth's dry atmosphere. [2, 15]

Gas	Symbol	Volume [%]	Concentration [ppm]
Nitrogen	N_2	78.08	-
Oxygen	O_2	20.95	-
Argon	Ar	0.93	-
Carbon dioxide	CO_2	0.0402	402
Neon	Ne	0.0018	18
Helium	He	0.0005	5
Methane	CH_4	0.00018	1.8

A large portion of the IR range is not useful in IR thermography because the IR attenuates due to absorption by gases and scattering by particles of the atmosphere. Atomic gases, such as Ar and diatomic gases of the same atomic species, such as N_2 and O_2, cannot absorb IR. However, molecules made up of two or more different atomic species, such as CO_2, CH_4 and H_2O, are able to absorb IR. The transmission of IR through the Earth's atmosphere in function of the wavelength, with the absorbing molecules is represented in Figure 2.5. Note that this measurement was done over a distance of 1250 m at 21 degrees Celsius and 100 % relative humidity. In the range between 5 and 8 μm, the transmission in wet air over a distance of 30 cm is still above 80 %. Hence, for lock-in IR thermography the sensitivity range of IR cameras might also reach into this range, which could be advantageous in achieving a higher sensitivity.

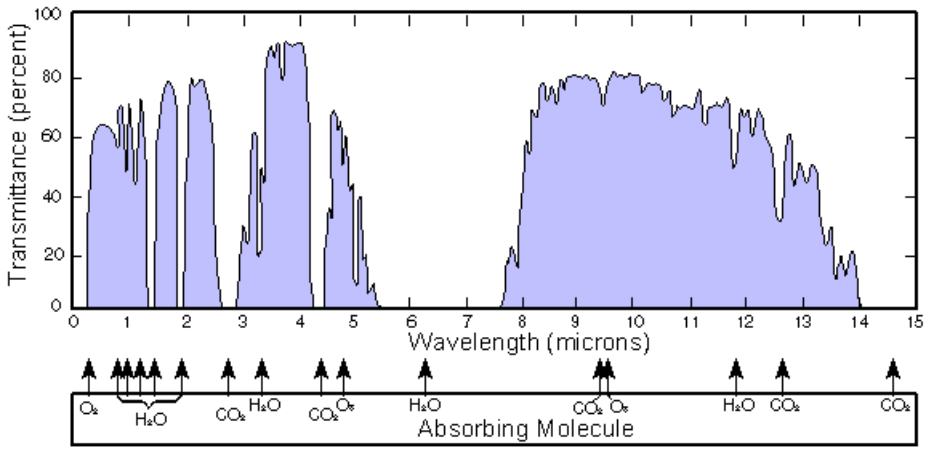

Figure 2.5: The atmospheric IR window with the absorbing molecules displayed. This measurement was done over a distance of 1250 m at 21 degrees Celsius and 100 % relative humidity. [16]

However, for most applications, the IR spectrum is divided in several subdivisions. This breakdown is dependent on the application, but a commonly used subdivision scheme is shown in Table 2.2. As depicted in Figure 2.5, the remaining portions, useful for IR thermography, are shown in Table 2.3.

Table 2.2: A Commonly used subdivision scheme for the IR spectrum. [17]

Division Name	Abbreviation	Wavelength [μm]
Near-IR	NIR	0.7 - 1.4
Short-Wavelength IR	SWIR	1.4 - 3
Mid-Wavelength IR	MWIR	3 - 8
Long-Wavelength IR	LWIR	8 - 15
Far-IR	FIR	15 - 1000

Table 2.3: The useful portions of the IR spectrum for IR thermography. [13]

Division Name	Abbreviation	Wavelength [μm]
Near-IR	NIR	0.7 - 1.4
Short-Wavelength IR	SWIR	1.5 - 2.5
Mid-Wavelength IR	MWIR	2.5 - 5
Long-Wavelength IR	LWIR	8 - 14

MWIR and LWIR are most commonly used in IR thermography because of two reasons:

1. range of peak emission: in order to obtain the most efficient measurement for a particular temperature, the measurement should be performed at the wavelength at which most intensity is emitted. Measuring at a different wavelength requires a much more sensitive camera to achieve identical performance. As a result of Wien's displacement law (discussed in Section 2.1.3, Equation 2.7), MWIR cameras are applied in high-temperature readings, while LWIR cameras are applied in ambient temperature readings.

2. atmospheric transmittance: as can be seen in Figure 2.5, the MWIR and LWIR are well transmitted through the Earth's atmosphere. [2, 5, 8, 12–17]

2.2 Infrared Thermography

2.2.1 Infrared Camera

The purpose of an IR camera is to convert IR into a false color visual image. This visual image represents the two-dimensional distribution of the IR emitted by an object or a scene. The main components of an IR camera are the optics, the IR detector, the electronics for signal or image processing and the user interface with output ports, control ports, and the image display. A simplified block diagram of the main components of an IR camera is shown in Figure 2.6. [2, 5]

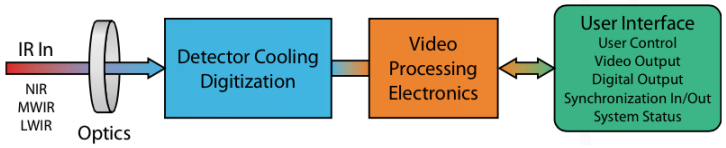

Figure 2.6: A simplified block diagram of the main components of an IR camera. [5]

2.2.2 Image Formation

The generation of thermal images is done according to two basic concepts, i.e. scanning systems and staring systems. For scanning systems, the IR is scanned in a raster scan pattern and the detected signal on the single IR detector element is combined with the position of the rotating mirrors in order to produce an image. This is shown in Figure 2.7a. For staring systems, every single detector element of the two-dimensional detector array provides information about the radiation at one point. This is shown in Figure 2.7b.

2.2.2.1 Scanning Systems

The scanning system has only one single IR detector element. This means that all images are built up sequentially. The setup in order to obtain a two-dimensional image is made up of two mirrors. A rotating mirror for horizontal scanning allows the radiation measurement along a horizontal line of the scene. A second mirror is used to switch the vertical position of the scanned line. This operating principle is shown in Figure 2.7a. In practice, this method is often combined with fast quantum detectors (discussed in Section 2.2.3) and short signal integration times (the time taken to scan a single full range spectrum) in order to obtain short image formation times at acceptable pixel numbers. Due to major improvements in the staring system technology, the limited number of pixels and the limited frame rates, scanning systems are not often used anymore. Nevertheless, scanning systems offer some advantages over staring systems, such as the accuracy, since the IR from all image pixels is detected by only one detector element. [2]

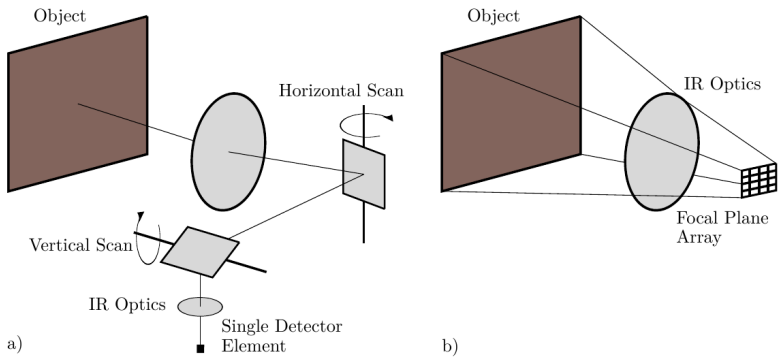

Figure 2.7: a) The operating principle of the scanning system. b) The operating principle of the staring system.

2.2.2.2 Staring Systems

General Aspects

The staring system has a two-dimensional array of single IR detector elements, which is called a focal plane array (FPA). This operating principle is shown in Figure 2.7b. FPA resolutions can range from about 40 x 40 pixels up to 1024 x 1024 pixels. This corresponds with a number of detectors that varies from 1,600 to more than 1,000,000. Here, every detector of the FPA provides information about the radiation at one point. Staring systems allow higher frame rates at higher pixel numbers than scanning systems.

Fundamentally, a FPA for IR imaging consists of two parts, i.e. the IR sensor made from an IR sensitive material and the readout integrated circuit (ROIC) made from silicon. ROICs have two functions. First, they realize the signal readout and second they contribute to the signal processing with the signal amplification and analog-to-digital conversion. Figure 2.8 shows a block diagram of a ROIC for a 1024 x 768 pixels bolometer array. The bolometer principle is discussed in Section 2.2.3.

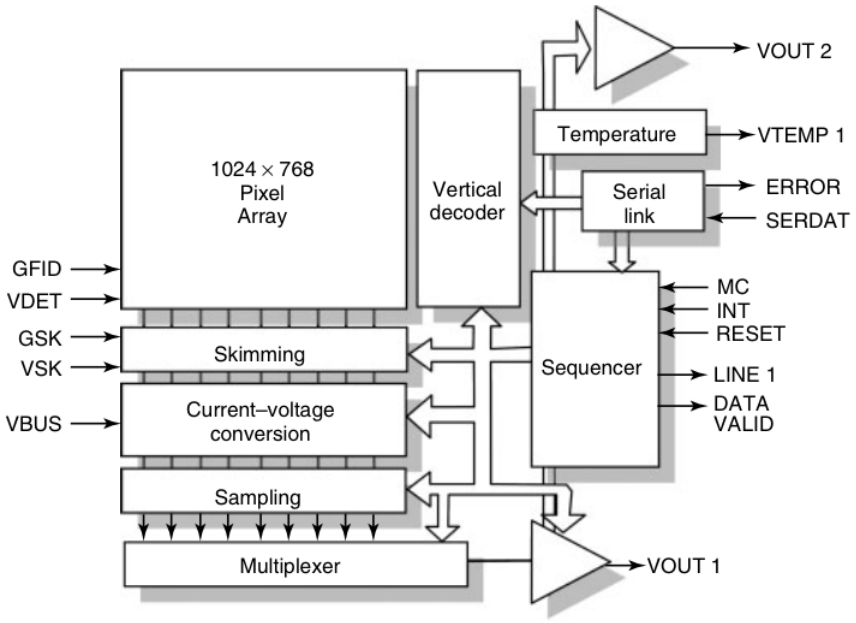

Figure 2.8: The block diagram of a ROIC for a 1024 x 768 pixels bolometer array. [2]

Today's characteristics of FPAs can be summarized as follows.

- The FPA resolutions can range from about 40 x 40 pixels up to 1024 x 1024 pixels. Figure 2.9 illustrates the different array sizes for a 1 megapixel image.
- The microbolometer FPA achieves a fill factor larger than 80 %, whereas quantum detector FPAs achieve a fill factor larger than 90 %. The fill factor is defined as the ratio between the IR sensitive cell area and the total cell area of an FPA. This is shown in Figure 2.10.
- The noise equivalent temperature difference (NETD) of today's IR cameras is able to achieve values of 45 mK for microbolometers and about 10 mK for quantum detectors. The NETD is the minimum temperature difference at two points of the image.
- The time response for microbolometer FPAs is about 10 ms. [2, 5, 13, 18]

Figure 2.9: A comparison of different array sizes for a 1 megapixel image. [2]

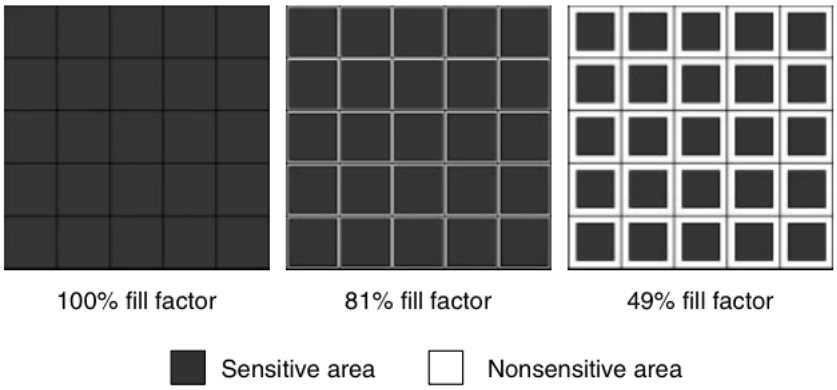

Figure 2.10: A representation of different values of the fill factor of an FPA displayed. [2]

Calibration Process

Since every IR detector element in the FPA has a slightly different gain and zero offset, these deviations must be corrected to a normalized value in order to create a useful thermographic image. This multi-step calibration process proceeds as follows:

1. the offset compensation brings each detector response within the dynamic range of the camera's A/D converter electronics, shown in Figure 2.11;
2. the slope correction brings all gain factors to the same value, shown in Figure 2.12;
3. the Non-Uniformity Correction (NUC) makes sure that all detectors have the same electronic characteristics, shown in Figure 2.13. [5, 13]

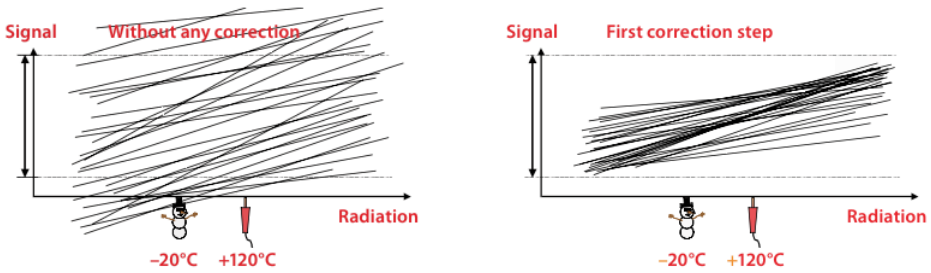

Figure 2.11: The figure on the left shows the outcome of every IR detector element without any correction. The figure on the right shows the result after the first correction step (offset compensation). [5]

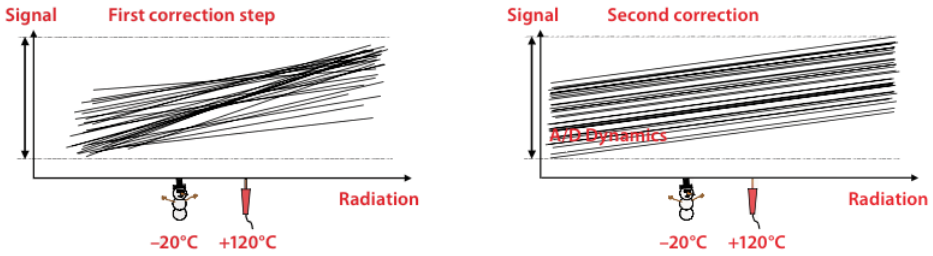

Figure 2.12: The figure on the left shows the outcome of every IR detector element after the first correction step (offset compensation). The figure on the right shows the result after the second correction step (slope correction). [5]

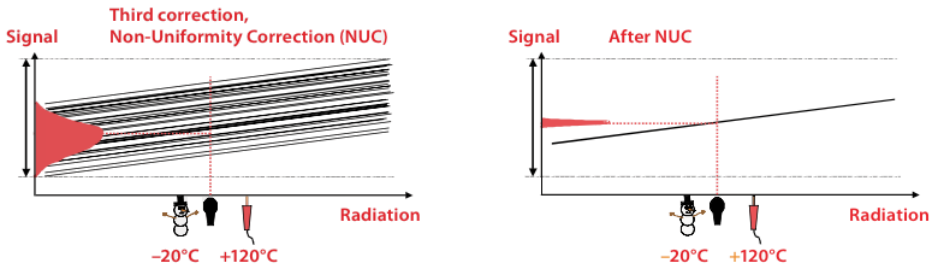

Figure 2.13: The figure on the left shows the outcome of every IR detector element after the second correction step (slope correction). The figure on the right shows the result after the third correction step (non-uniformity correction). [5]

2.2.3 Detectors

IR detector technologies can be divided into two operating principles, i.e. non-quantum detectors and quantum detectors. Non-quantum detectors (or thermal detectors) convert the IR into an electrical signal in two steps. First, the incident radiation is absorbed, which causes a change of temperature of the IR absorbing material. Second, the electrical output of the non-quantum sensor is produced by a change in some physical property of the IR absorbing material, caused by the change of temperature. Quantum detectors (or photon detectors) convert the IR into an electrical signal directly. This is obtained due to absorption of photons from the IR, which causes a changes of mobility of the free charge carriers in the detector element. If the incident radiation generates non-equilibrium charge carriers, the electrical resistance of the detector element is changed or an additional photocurrent is generated. [2]

2.2.3.1 Non-Quantum Detectors

A commonly used type of a non-quantum detector is an uncooled microbolometer. The operating principle of an uncooled microbolometer is based on a temperature-dependent resistor. First, the incident radiation is absorbed, which causes a change of temperature of the microbolometer element (IR absorbing material made of a metal or a semiconductor material). A simplified representation of a microbolometer element is shown in Figure 2.14.

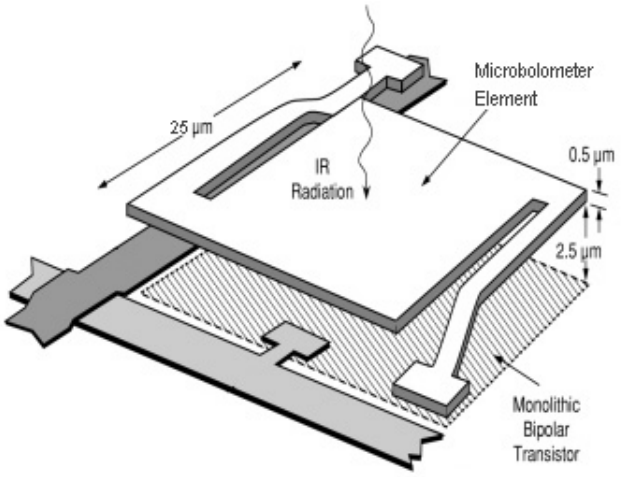

Figure 2.14: A representation of a microbolometer element. An array up to 1024 x 1024 elements is used in FPA detectors. [19]

The change of temperature ($\triangle T$) of the microbolometer element, for a square-wave pulse of radiation, is given by following equation:

$$\triangle T = \frac{\alpha \Phi_0}{G_{th}}(1 - e^{-\frac{t}{\tau}}) \tag{2.13}$$

Where $\triangle T$ is expressed in $[K]$, Φ_0 is the radiation power ($\Phi_0 = \Phi_{object} - \Phi_{detector}$), G_{th} is the heat conductance, t is the time and τ is the time constant ($\tau = \frac{C_{th}}{G_{th}}$, where C_{th} is the heat capacitance). As can be derived from Equation 2.13, the change in detector temperature exhibits an exponential rise and decay.

The electrical output of the microbolometer sensor is produced by a change of resistance of the microbolometer element, caused by the change of temperature. This change of resistance ($\triangle R$) can be expressed as follows:

$$\triangle R = \overline{\beta R}\, \triangle T \tag{2.14}$$

Where $\triangle R$ is expressed in $[\Omega]$ and $\overline{\beta R}$ is the average temperature coefficient in the temperature interval $\triangle T$.

This change of resistance of the microbolometer element can be expressed with the absorbed radiant power $\alpha \Phi_0$ for steady-state conditions:

$$\triangle R = \frac{\overline{\beta R} \alpha \Phi_0}{G_{th}} \tag{2.15}$$

From Equation 2.15, it is clear that the change of resistance of the microbolometer element is proportional with the incident radiation power.

Low sensitivities, broad spectral response and slow response times in the order of 10 ms characterize the microbolometer. Bolometers do not offer the possibility to set the integration time, because they operate as thermal detectors. The integration time is given by the thermal time constant of the bolometer detector. Figure 2.15 shows the signal generation process and signal readout in a bolometer camera. The image formation of microbolometer FPA cameras is obtained by sequential readout of the detector lines, which is called rolling readout. [2, 5, 13, 19]

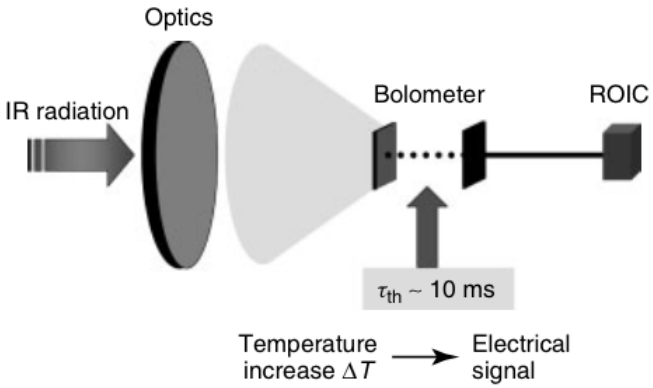

Figure 2.15: The signal generation process and signal readout in a bolometer camera. The dotted line represents the thermal capacitance. [2]

2.2.3.2 Quantum Detectors

General Aspects

For more demanding applications, quantum detectors are used. Quantum detectors convert the absorbed IR directly into a change of some electrical property. This is obtained by the change of the free charge carrier concentration in a semiconductor, which is called 'the intrinsic photoelectric effect'. Solids as semiconductors have a typical electronic band structure (with a valence band and a conduction band) and an energy gap. This band structure is represented in Figure 2.16a. In order to obtain an electronic transition between the valence band and the conduction band, the quantum energy of the incident photon ($E = hf$) must exceed an energy threshold ($\triangle E$). Thus, for the intrinsic photoelectric effect, the interband excitation of an electron-hole pair at photon energies exceeds the energy gap of the semiconductor. This operating principle is represented in Figure 2.16b. Since quantum detectors operate with an energy threshold, the spectral sensitivity region is limited by a cutoff wavelength:

$$\triangle E = hf_{cutoff} = \frac{hc}{\lambda_{cutoff}} \tag{2.16}$$

Where $\triangle E$ is expressed in $[meV]$. The quantum detector is only sensitive for $\lambda \leq \lambda_{cutoff}$. From this, it is clear that the sensitivity of the detector is strongly dependent on the incident wavelength.

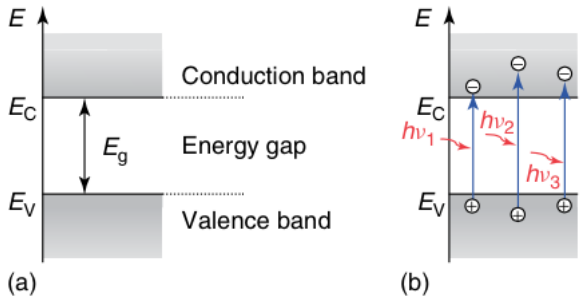

Figure 2.16: a) A simplified energy-band structure of solids. b) The intrinsic photoelectric effect for varying energy levels. [2]

Quantum detector cameras offer smaller NETD values and higher frame rates than microbolometer cameras, because photodiode arrays offer time constants down to 1 μs. Snapshot operation of quantum detector FPA cameras is possible due to direct conversion of the photon flux into a photocurrent and the small time constant. Quantum detector cameras offer the possibility to set the integration time, which is obtained due to the charging of a capacitor by the photocurrent of each pixel. The signal generation process and signal readout in a quantum detector camera is shown in Figure 2.17. [2, 5, 13, 19–21]

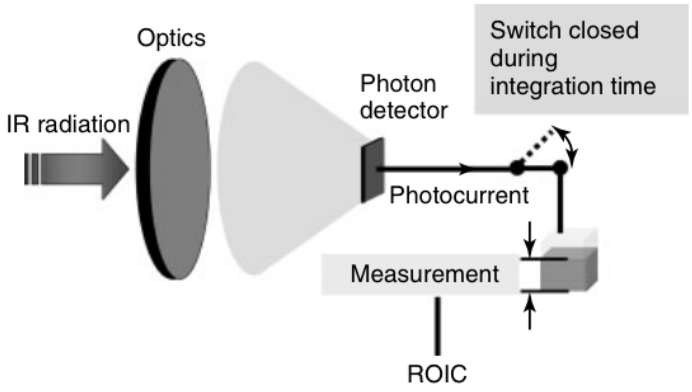

Figure 2.17: The signal generation process and signal readout in a quantum detector camera. [2]

Quantum detectors can be subdivided into different types, depending on the operation principle. The most important quantum detectors are:

- photoconductors, made of indium antimonide ($InSb$);
- photodiodes, made of mercury cadmium telluride ($HgCdTe$ - MCT) or indium gallium arsenide ($InGaAs$);
- Schottky barrier detectors, made of platinum silicide ($PtSi$);
- quantum well infrared photodetectors ($QWIPs$), made of layered gallium arsenide/aluminum gallium arsenide ($GaAs/AlGaAs$).

Each detector type ensures another sensitivity for a certain wavelength. This is represented in Figure 2.18. [2, 5, 13, 19–21]

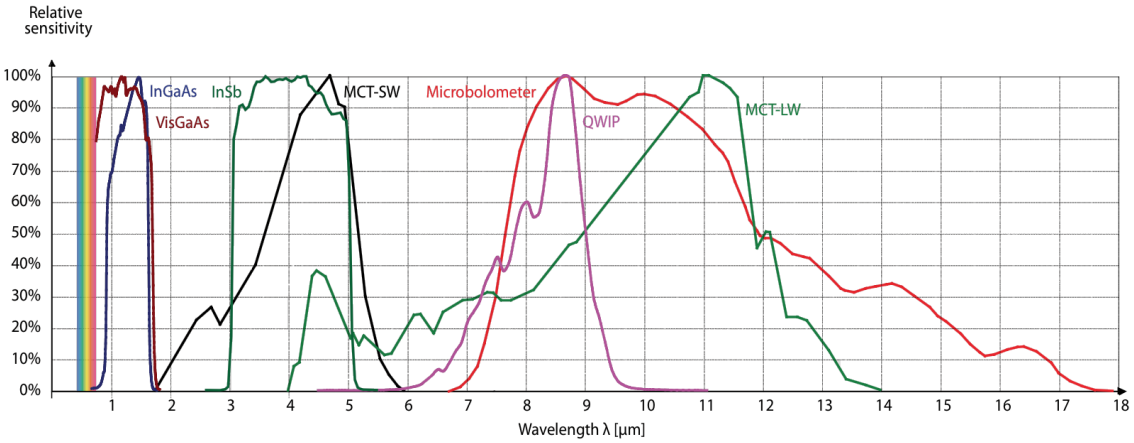

Figure 2.18: The relative response curves for different detector types. [5]

Cooling Aspects

By cooling down quantum detectors to low temperatures, the free charge carrier concentration decreases and therefore the noise of the detector decreases. For MWIR and LWIR, the FPA is cooled down to 77 K. For SWIR, the FPA is cooled down to 200 K. Table 2.4 shows the most commonly used detectors in today's IR cameras, with their operation spectra and operating temperatures.

Because FPAs are small, the attachment area and the cooler itself can be relatively small. Different cooling methods can be applied to cool quantum detectors, whereof the most commonly used ones can be summarized as follows:

- a nitrogen Dewar flask attached to the detector, keeping the detector at a very stable and low temperature (77 K);
- a Peltier cooler, based on the Peltier effect, is a solid-state solution where a direct current is forced through a thermoelectric material, which creates a hot and a cold side (200 K);
- a Stirling cooler is based on the compression (heating) and expansion (cooling) of gases, which leads to a hot and a cold side (70 K). [2, 5, 13, 19–21]

Table 2.4: The most commonly used detectors in today's IR cameras, including their operating spectra and temperatures. [5]

Detector Type / Material	Operation	Operating temperature
Microbolometer	Broadband Detector	Uncooled ($\approx$ 300 K)
InSb	MWIR Quantum Detector	77 K
HgCdTe	SWIR Quantum Detector	200 K
HgCdTe	LWIR Quantum Detector	77 K
PtSi	MWIR Quantum Detector	77 K
QWIP	LWIR Quantum Detector	70 K

2.2.4 Digitization

The IR intensity of the target object can be described as a function with two variables (f(x, y)). The amplitude f is a scalar positive value, which corresponds with the amount of energy radiated from the target object at spatial coordinates (x, y). An example of an object's emitted IR, shown as a three-dimensional function, is displayed in Figure 2.19. The function f must be sampled in both space and amplitude in order to convert the function to a digital format. Sampling is the digitization of the image space, whereas quantization is the digitization of the amplitude.

The resolution of the IR camera defines sampling and describes the amount of individual IR detectors on the FPA. Usually, it is displayed as M x N, where M stands for the number of rows and N stands for the number of columns. A typical value of camera resolution is 1024 x 1024, i.e. more than 1,000,000 individual detectors.

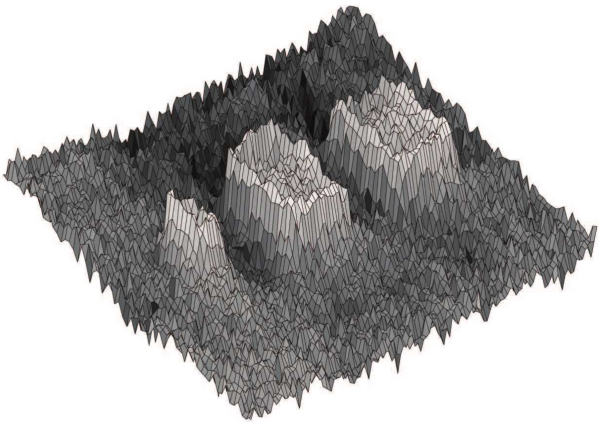

Figure 2.19: An example of an object's emitted IR, shown as a three-dimensional function. [22]

Three aspects define quantification:

1. the bit depth, which is the number of bits used to display a discrete value. A typical value of bit depth is 14 bits, i.e. 16,384 levels.

2. the sensitivity, which is the minimum temperature difference at two points in the IR image. This is commonly expressed as the NETD. A typical value of NETD for IR cameras is 20 mK.

3. the frame rate, which is the number of images or frames an IR camera can acquire per second. A typical value of frame rate is 60 Hz. However, acquiring only from a region of the frame will increase the frame rate significantly: up to 30 kHz for some cameras. [2, 13, 22]

2.2.5 Field of View

The field of view (FOV) is the angular size of the object field that can be observed by the camera. This is shown in Figure 2.20.

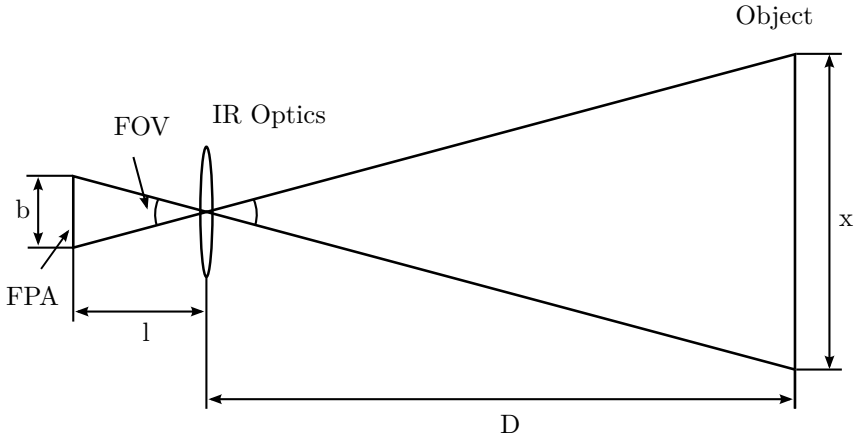

Figure 2.20: A representation of the cross section of the FOV.

The FOV depends on the camera lens and the FPA dimensions. The rays that hit the four edges of the detector array limit the FOV. The formula to determine the FOV can be easily constructed with some basic trigonometrical concepts:

$$FOV = 2 \arctan\left(\frac{b}{2l}\right) \tag{2.17}$$

Where FOV is expressed in $[rad]$, l is the focal length of the camera lens and b is the dimension of the FPA in one direction. The rectangular shape of the FPA causes a horizontal FOV (HFOV) and a vertical FOV (VFOV). The observed length (x) of a scene at a given object distance (D), can be calculated as follows:

$$x = 2D \tan\left(\frac{FOV}{2}\right) \tag{2.18}$$

Where x is expressed in $[m]$. The same applies to one detector element of the focal plane array, where the instantaneous FOV (IFOV) presents the angle over which one detector element senses the target object's radiation. From here, using the small angle approximation, the minimal object size (d) the camera can detect is given by following equation:

$$d = IFOV * D \tag{2.19}$$

Where d is expressed in $[m]$. [2]

2.2.6 Temperature Measurements

The camera can convert incident IR into a temperature value. However, the total incident radiation on the camera lens (M_{tot}) originates from three different sources, i.e. the target object's radiation (M_{obj}), the radiation coming from the object surroundings that reflects in the camera lens (M_{refl}) and the atmospheric radiation (M_{atm}). This is shown in Figure 2.21. Since only the target object's temperature is important, the total camera output must be compensated. The knowledge obtained in section 2.1.3 allows us to derive a formula for the calculation of the target object's temperature from a calibrated camera output.

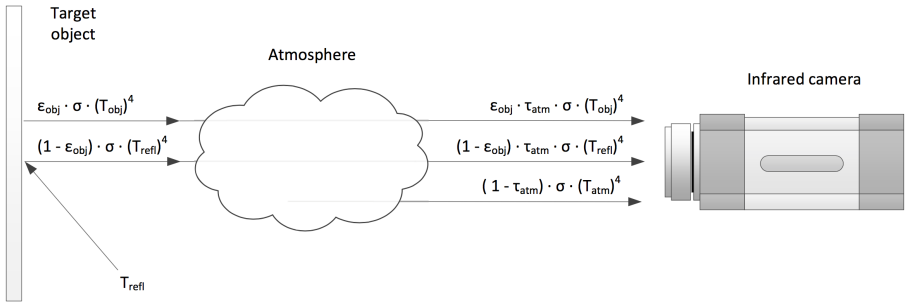

Figure 2.21: The total incident radiation on the IR camera lens originates from the target object, reflections and the atmosphere. [13]

The total incident radiation on the IR camera lens:

$$M_{tot} = M_{obj} + M_{refl} + M_{atm} \tag{2.20}$$

The first source is the emission of the target object. As discussed in Section 2.1.5, some of the emitted radiation will be absorbed by gases and scattered by particles of the atmosphere. Therefore, it is necessary to take into account the transmittance of the atmosphere ($\boldsymbol{\tau}_{atm}$). So, the incident radiation on the camera lens of the target object can be expressed as follows:

$$M_{obj} = \varepsilon_{obj} * \boldsymbol{\tau}_{atm} * \sigma * (T_{obj})^4 \tag{2.21}$$

The radiation coming from the target object surroundings that reflects in the camera lens can be expressed as follows, where $\rho_{obj} = 1 - \varepsilon_{obj}$ (Section 2.1.4, Equation 2.11):

$$M_{refl} = \rho_{obj} * \boldsymbol{\tau}_{atm} * \sigma * (T_{refl})^4 = (1 - \varepsilon_{obj}) * \boldsymbol{\tau}_{atm} * \sigma * (T_{refl})^4 \tag{2.22}$$

The third component is the atmospheric radiation. Both the emitted radiation of the target object and the reflected radiation become attenuated when they pass through the atmosphere. Since the atmosphere absorbs a part of the radiation, it will radiate some itself (Kirchhoff's law). This can be expressed by following equation, where $(1 - \boldsymbol{\tau}_{atm})$ is the emittance of the atmosphere:

$$M_{atm} = \varepsilon_{atm} * \sigma * (T_{atm})^4 = (1 - \boldsymbol{\tau}_{atm}) * \sigma * (T_{atm})^4 \tag{2.23}$$

Substituting Equation 2.21-2.23 in Equation 2.20 provides a more detailed expression of the total incident radiation on the camera lens:

$$M_{tot} = \varepsilon_{obj} * \boldsymbol{\tau}_{atm} * \sigma * (T_{obj})^4 + (1 - \varepsilon_{obj}) * \boldsymbol{\tau}_{atm} * \sigma * (T_{refl})^4 + (1 - \boldsymbol{\tau}_{atm}) * \sigma * (T_{atm})^4 \tag{2.24}$$

Equation 2.24 can be solved to the temperature:

$$T_{obj} = \sqrt[4]{\frac{M_{tot} - (1 - \varepsilon_{obj}) * \boldsymbol{\tau}_{atm} * \sigma * (T_{refl})^4 - (1 - \tau_{atm}) * \sigma * (T_{atm})^4}{\varepsilon_{obj} * \boldsymbol{\tau}_{atm} * \sigma}} \tag{2.25}$$

In order to solve Equation 2.25, we need the target object's emissivity (ε_{obj}), the reflected temperature (T_{refl}), the transmittance of the atmosphere ($\boldsymbol{\tau}_{atm}$) and the temperature of the atmosphere (T_{atm}). [2, 5, 13]

2.2.7 Advantages and Disadvantages

The advantages of IR thermography include:

- the possibility to compare temperatures over a large area;
- the possibility to catch moving targets in real time;
- the possibility to detect objects in dark areas;
- the non-contact observation method;
- the usage as a non-destructive testing method.

The disadvantages of IR thermography include:

- the price of a quality IR camera rises quickly to a few thousand euros;
- the detection of subsurface temperatures is not possible;
- the temperature measurements are not as accurate as contact methods;
- the temperature measurements are often incorrect without a correct calibration for emissivity, distance, ambient temperature and relative humidity. [23–26]

2.3 Lock-In Infrared Thermography

2.3.1 Non-Destructive Testing

Non-destructive testing (NDT) is a wide group of methods used for the analysis of material characteristics of a test specimen without damaging the material or affecting its properties. Since NDT does not permanently alter the test specimen, it is a valuable testing method that can save both time and money in research, troubleshooting and product evaluation. NDT is commonly used in engineering, medicine and art. Different NDT techniques include, but are not limited to, ultrasonic testing, radiographic testing, magnetic-particle inspection, liquid penetrant testing, and IR thermography. [22, 27]

2.3.2 Infrared Thermography in Non-Destructive Testing

In general, two modes are used when performing NDT with IR thermography, i.e. passive mode and active mode. In passive mode, the test specimen is observed by an IR camera without adding an external excitation source to induce a noticeable temperature variation. This is shown in Figure 2.22. The data analyzer is optional if the IR camera does not have the ability to represent the image with a user interface. Defective areas are naturally at a higher temperature than the environment. Potential problems relevant to detect are indicated by abnormal temperature profiles. In passive IR thermography, a temperature difference compared to the environment of 4°C is an indication of an underlying defect. Passive IR thermography provides a qualitative, but not a quantitative indicator of the defect.

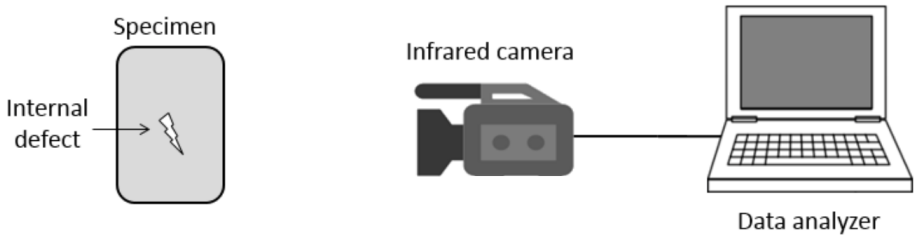

Figure 2.22: The fundamental setup to perform passive IR thermography for NDT. The main components are an IR camera and an optional data analyzer.

In active mode, the test specimen is observed by an IR camera while an external excitation source is added in order to induce a noticeable temperature variation. This is shown in Figure 2.23. The data analyzer is necessary to compute the data images, regardless of whether or not the camera has a user interface. The thermal variation can be obtained by means of different excitation ways, i.e. electrical excitation, optical excitation, ultrasonic excitation, etc. Active IR thermography is divided in different subclasses based on the excitation method, i.e. vibrothermography, pulsed IR thermography and lock-in IR thermography. Active IR thermography is a quantitative measurement, since it is possible to estimate the defect properties, such as the defect type, the defect dimensions, the defect location, the defect depth, etc. [12, 22]

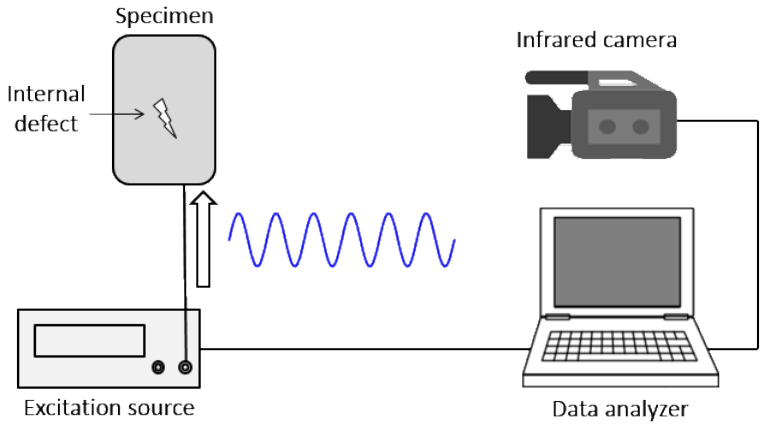

Figure 2.23: The fundamental setup to perform active IR thermography for NDT. The main components are an IR camera, an excitation source and a data analyzer.

2.3.3 Lock-In Infrared Thermography as Non-Destructive Test

Lock-in IR thermography is a commonly used NDT method, which is able to evaluate subsurface material characteristics. The evaluated material characteristics include minor subsurface defects, which are not visible for the naked eye. The lock-in IR thermography principle is based on the excitation of a periodic thermal signal to the test specimen. Typically, a sinusoidal excitation signal is used for the generation of the thermal fluctuation in the test specimen. Nevertheless, for practical reasons, a square excitation signal or a triangle excitation signal can also be applied. The lock-in algorithm will only extract the thermal signal fluctuating with the lock-in frequency and analyze its properties in order to access the material characteristics. Figure 2.23 represents a possible hardware setup to perform lock-in IR thermography. [12, 28, 29]

2.3.3.1 General Aspects

Defect Depth

Since thermal signals are highly attenuated, it is only possible to detect subsurface defects which are lying just underneath the surface of the test specimen. The absolute temperature T on time t and the depth z is formulated as follows:

$$T(z,t) = T_0 e^{-\frac{z}{\mu}} cos\left(\omega t - \frac{2\pi z}{\lambda}\right) \tag{2.26}$$

Where $\lambda = 2\pi\mu$ and μ is the thermal diffusion length, which is given by following equation:

$$\mu = \sqrt{\frac{2\varsigma}{\omega}} \tag{2.27}$$

Where μ is expressed in $[m]$ and ς is the thermal diffusivity, which can be represented as follows:

$$\varsigma = \frac{\kappa}{\varrho c_p} \tag{2.28}$$

Where ς is expressed in $[\frac{m^2}{s}]$, κ is the thermal conductivity, ϱ is the mass density and c_p is the specific heat capacity.

The thermal diffusion length (Equation 2.27) is the distance where the amplitude of the thermal signal is degraded to a value of e-times smaller. The value of μ is inversely proportional to $\sqrt{\omega}$. Therefore, signals with a lower frequency penetrate more deeply in materials than signals with higher frequencies. Thus, it is very important to apply an optimal lock-in frequency in order to detect every possible defect. The optimal lock-in frequency is dependent on both the thermophysical characteristics and the thickness of the test specimen.

In practice, the lock-in frequency that can be applied depends on the frame rate of the IR camera and must comply with following equation:

$$f_{lock-in} \leq \frac{f_{fr}}{n} \tag{2.29}$$

Where $f_{lock-in}$ is expressed in $[Hz]$ and n is the number of frames evaluated in every lock-in period. According to the Nyquist-Shannon sampling theorem, at least two samples per lock-in period are necessary. Because two-phase correlation is used, at least four frames have to be evaluated for every lock-in period. Therefore, the maximum usable lock-in frequency is a quarter of the frame rate of the camera. Nevertheless, a lower lock-in frequency can be used by increasing the evaluated frames per lock-in period. For each lock-in frequency, another test has to be done, which is the main disadvantage of lock-in IR thermography.

The main advantage of lock-in IR thermography is the fact that the phase is independent of non-uniform heating or local optical surface features, such as emissivity. The phase depends directly on the defect depth, which can be derived from Equation 2.26:

$$\phi(z) = \frac{2\pi z}{\lambda} = \frac{z}{\mu} \tag{2.30}$$

Where $\phi(z)$ is expressed in $[rad]$. Provided formulas are applicable when a one-dimensional model for half space is heated with a sinusoidal changing intensity. [12, 28–31]

Sensitivity
The sensitivity of lock-in IR thermography can be described as the signal to noise ratio (SNR), which is formulated as follows:

$$SNR = \frac{\triangle T_{signal}}{\triangle T_{noise}} \tag{2.31}$$

Where $\triangle T_{signal}$ is the temperature amplitude of the test specimen and $\triangle T_{noise}$ is the temperature amplitude of the noise in the data images. $\triangle T_{signal}$ is proportional to the applied excitation power (P), the properties of the test specimen, i.e. the absorption factor (α), the heat conductance (G_{th}) and the heat capacitance (C_{th}), and the duration of exposure (t). This is represented for a square-wave pulse of radiation by following equation:

$$\triangle T_{signal} = \frac{\alpha P}{G_{th}}(1 - e^{-\frac{t}{\tau}}) \tag{2.32}$$

$\triangle T_{noise}$ is dependent on both the IR camera's properties, i.e. the NETD and frame rate (f_{fr}), and the measurement time (t_{meas}). This relation is represented as follows:

$$\triangle T_{noise} = NETD * \frac{2}{\sqrt{f_{fr} * t_{meas}}} \tag{2.33}$$

Hence, the SNR can be increased by increasing $\triangle T_{signal}$ or by reducing $\triangle T_{noise}$. $\triangle T_{signal}$ can be increased by increasing the excitation power or by increasing the exposure duration (applying a lower frequency). $\triangle T_{noise}$ can only be reduced by increasing t_{meas} since the IR camera's properties are fixed. So, in order to obtain a satisfactory result after a very short period ($\approx$ 1 s), the IR camera's NETD has to be low ($<$ 20 mk) and the frame rate has to be high ($>$ 100 Hz). Therefore, MCT or InSb quantum IR cameras (discussed in Section 2.2.3) are recommended to perform lock-in IR thermography. [12, 28–31]

2.3.3.2 Discrete Fourier Transform

General Aspects

As can be inferred from the above mentioned, the amplitude (modulus) and the phase of the thermal signal provides important information. To obtain these parameters, a discrete Fourier transformation (DFT) is performed at one frequency (the lock-in frequency) at every spatial point. This principle is shown in Figure 2.24 and is formulated as follows:

$$F_{(f)} = \sum_{t=0}^{N-1} \frac{f_{(t)} e^{-j2\pi ft}}{N} = \sum_{t=0}^{N-1} \frac{f_{(t)} cos(j2\pi ft)}{N} - \sum_{t=0}^{N-1} \frac{f_{(t)} sin(j2\pi ft)}{N} \tag{2.34}$$

Where N is the total number of frames evaluated during the processing. As can be seen, $F_{(f)}$ is a complex number that encodes both the amplitude and the phase of a sinusoidal component of function $f_{(t)}$. The amplitude at every spatial point provides information about the dissipated power and can be found by following equation:

$$A = \sqrt{\Re^2 + \Im^2} \tag{2.35}$$

Where $\Re$ is the real part of $F_{(f)}$ and $\Im$ is the imaginary part of $F_{(f)}$. The phase at every spatial point can be found by following equation:

$$\phi = tan^{-1}\left(\frac{\Im}{\Re}\right) \tag{2.36}$$

[12, 28–33]

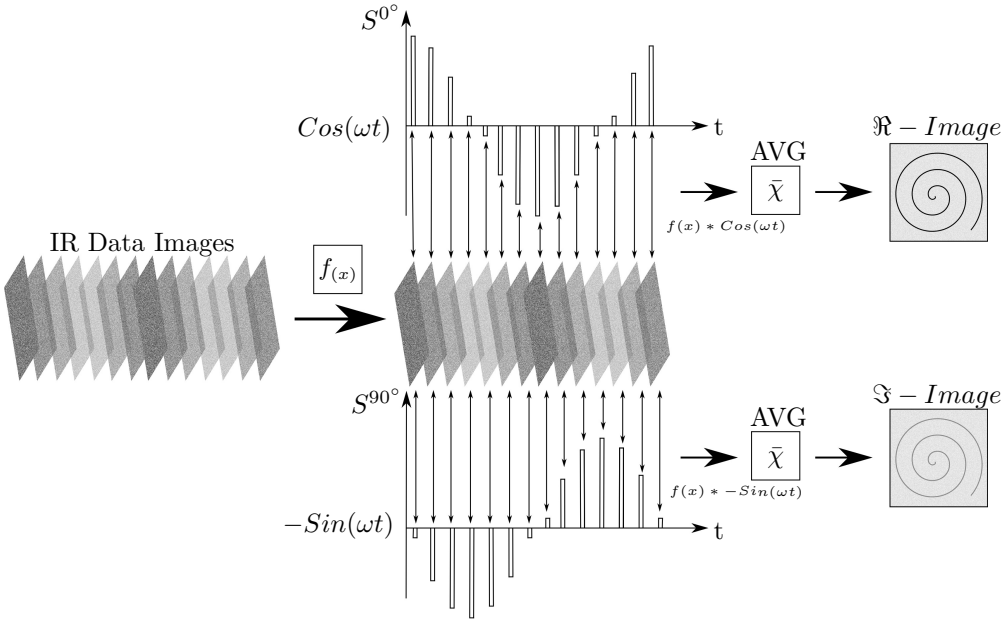

Figure 2.24: A representation of the lock-in principle. Basically, a DFT is performed at one frequency (the lock-in frequency) at every spatial point. After this process, the real and imaginary images are obtained.

Averaging

Two averaging methods are commonly used in lock-in IR thermography, i.e. continuous averaging and moving averaging. The continuous averaging method is an average of several data points without having a fixed subset. The more data points are included, the more accurate the average will be. However, in case something happens for a short period of time during the measurement, it will not be included in the total continuous average. In this case, the moving averaging method will be applied. The moving averaging method is an average of several data points with a fixed subset. This subset is determined by the desired number of lock-in periods in the average. [12, 28–32]

2.3.3.3 Application

For example, given a sinusoidal thermal signal with an amplitude of 4 K and a frequency of 0.16 Hz, as represented in Figure 2.26a. When this thermal signal is subjected to a DFT with a lock-in frequency of 0.16 Hz, the real part of the DFT is calculated by multiplying the thermal signal with $\cos(2 * \pi * 0.16 * t)$, as represented in Figure 2.26b. The outcome is a superimposed sinusoidal signal with an amplitude of 2 K, an offset of 2 K and fluctuating at a frequency of 0.16 Hz, which is represented in Figure 2.26c. It is clear that the average of the latter is 2 K. When the modulus and the phase calculations have been carried out, this part will show in the results. It can be concluded that the thermal signal fluctuates at the lock-in frequency since the average of the DFT (the real part) does not equal zero. The same principle applies to the imaginary part of the DFT.

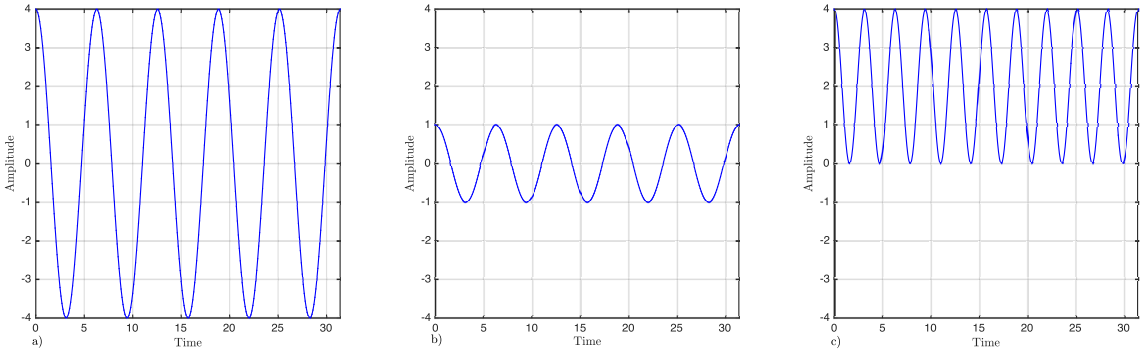

Figure 2.25: a) The incoming thermal signal with a frequency of 0.16 Hz (4*cos$(2 * \pi * 0.16 * t)$). b) The weighting factors for the calculation of the real part of the DFT with a lock-in frequency of 0.16 Hz (cos$(2 * \pi * 0.16 * t)$). c) The resulting signal, which is the real part of the DFT (4*cos$(2 * \pi * 0.16 * t)$ * cos$(2 * \pi * 0.16 * t)$).

The opposite can also be demonstrated. For example, given a sinusoidal thermal signal with an amplitude of 4 K and a frequency of 0.32 Hz, as represented in Figure **??**a. When this thermal signal is subjected to a DFT with a lock-in frequency of 0.16 Hz, the real part of the DFT is calculated by multiplying the thermal signal with $\cos(2 * \pi * 0.16 * t)$, as represented in Figure **??**b. The outcome is a periodic signal with peaks up to 4 K and fluctuating at a frequency of 0.16 Hz, as represented in Figure **??**c. However, the signal is now symmetric with respect to the time axis. Therefore, after averaging this signal, the outcome will be zero. It can be concluded that the thermal signal does not fluctuate at the lock-in frequency since the average of the DFT (the real part) equals zero. The same principle applies to the imaginary part of the DFT.

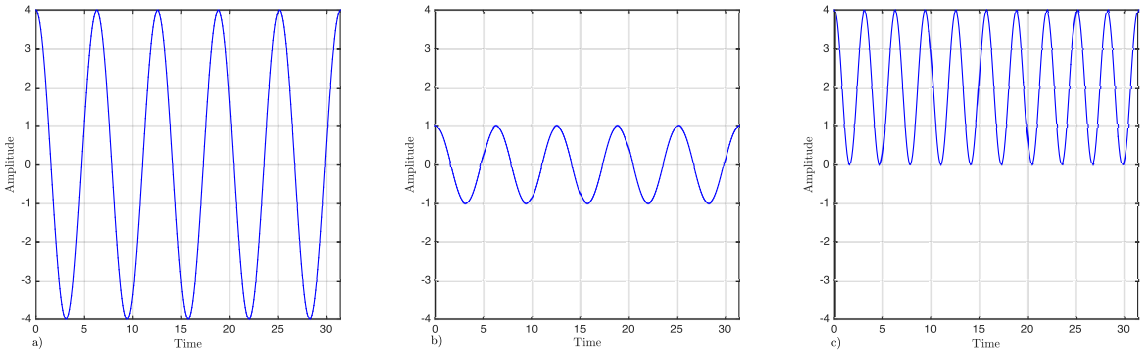

Figure 2.26: a) The incoming thermal signal with a frequency of 0.16 Hz (4*cos$(2 * \pi * 0.16 * t)$). b) The weighting factors for the calculation of the real part of the DFT with a lock-in frequency of 0.16 Hz (cos$(2 * \pi * 0.16 * t)$). c) The resulting signal, which is the real part of the DFT (4*cos$(2 * \pi * 0.16 * t)$ * cos$(2 * \pi * 0.16 * t)$).

2.3.4 Advantages and Disadvantages

The advantages of lock-in IR thermography include:

- the algorithm causes a noise-filter;
- the sensitivity is 100 to 1,000 times greater than the best thermal cameras;
- the phase image is insensitive to external influences;
- the phase image is insensitive to uneven distribution of the applied heat;
- the examination area can be large and measured from a distance;
- the heat sources are widely available and affordable;
- the visualization of deeper defects is better than with pulse IR thermography.

The disadvantages of lock-in IR thermography include:

- the operating principle is slower than other approaches;
- the bandwidth is limited to one frequency per test;
- the hardware setup is very expensive. [34, 35]

Chapter 3

Materials and Methods

3.1 Hardware

3.1.1 Infrared Camera

Two IR cameras were used during this master's thesis to perform lock-in IR thermography, i.e. the FLIR A5sc and the FLIR E40, purchased from FLIR Systems Inc. (Wilsonville, OR, USA). These IR cameras are respectively shown in Figure 3.1a and Figure 3.1b. The FLIR A5sc IR camera was used when a high frame rate (60 Hz) or a small minimum focus distance (5 mm) was needed. The compact design allows the camera to be placed at locations with limited space. This FLIR A5sc IR camera has two major disadvantages. The resolution is limited to 80 x 64 pixels and the camera requires an additional data analyzer in order to capture and save data images. The FLIR E40 IR camera was used when a higher resolution (320 x 245) was needed. This camera has a user interface and an internal memory, which allows the user to capture and save data images without an external data analyzer. The disadvantages of this camera are the minimum focus distance of 0.4 m and the low frame rate (7.5 Hz). The specifications of the FLIR A5sc and the FLIR E40 IR camera are shown in table 3.1. [36–39]

Figure 3.1: a) The FLIR A5sc IR camera. b) The FLIR E40 IR camera. [36, 37]

Table 3.1: The specifications of the FLIR A5sc IR camera and the FLIR E40 IR camera. [36,38,39]

Features	FLIR A5sc	FLIR E40
Detector Type	Uncooled VOX Microbolometer	FPA, Uncooled Microbolometer
Spectral Range	7.5 μm to 13.0 μm	7.5 μm to 13.0 μm
Resolution	80 x 64	160 x 120
NETD	$<$ 50 mK	$<$ 70 mK
Frame Rate	60 Hz	60 Hz
Dynamic Range	14-Bit	14-Bit
Command and Control	Gigabit Ethernet	USB-mini, USB-A, Composite Video, Bluetooth, Wi-Fi
Accuracy	$\pm$ 5°C	$\pm$ 2°C
Lens	5 mm	15° Telephoto Lens 45° Wide Angle Lens
Focus	Fixed	Manual
Operating Temperature Range	-40°C to 70°C	-20°C to 650°C
Dimensions w/o Lens	106 x 40 x 43 mm	246 x 97 x 184 mm

3.1.2 Excitation Source

3.1.2.1 Function Generator

The Keithley 3390 Arbitrary Waveform/Function Generator, purchased from Keithley Instruments Inc. (Cleveland, OH, USA), was used during the lock-in IR thermography experiments with electrical and optical excitation and is shown in Figure 3.2. The function generator was used for the generation of the lock-in signal (sine wave, block wave or triangle wave) at frequencies ranging from 0.01 Hz to 1 Hz. This corresponds with time periods of the lock-in signal ranging from 1 s to 100 s. It must be taken into account that the function generator cannot deliver sufficient power to generate a noticeable thermal fluctuation in the test specimen. Therefore, the output signal of the function generator was amplified 6.6 times with a custom-made power amplifier, which is discussed in detail in Section 4.1.1. [40, 41]

Figure 3.2: The Keithley 3390 Arbitrary Waveform/Function Generator as used during the lock-in IR thermography experiments with electrical and optical excitation. [41]

3.1.2.2 Power LED

General Aspects

Four LED Engin LZ9-00CW00 power LEDs, purchased from LED Engin Inc. (San Jose, CA, USA), were used during the lock-in IR thermography experiments with optical excitation. Figure 3.3 represents one such power LED as used in the lock-in IR thermography experiments. These Power LEDs, each consisting of an array of nine LEDs, were rated at a maximum power of 20 W. Therefore, the total maximum power available for the lock-in IR thermography experiments with optical excitation was 80 W.

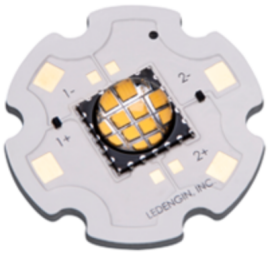

Figure 3.3: The LED Engin LZ9-00CW00 power LED as used during the lock-in IR thermography experiments with optical excitation. [42]

The relative spectral power in function of the wavelength of the power LEDs is represented in Figure 3.4. This figure shows that the spectral power peak of the power LEDs is located at 450 nm. This is an important factor since the test specimen has to absorb EM waves with this wavelength. The relative spectral power also shows that the power LEDs emit virtually no IR. This is important since all emitted IR can be reflected on the sample and interfere with the signal captured by the IR camera. However, some IR will be emitted since the power LEDs heat up due to the Joule effect. In order to mitigate the heating, the power LEDs are mounted on a heat sink and a glass plate is placed between the power LEDs and the test specimen. [42]

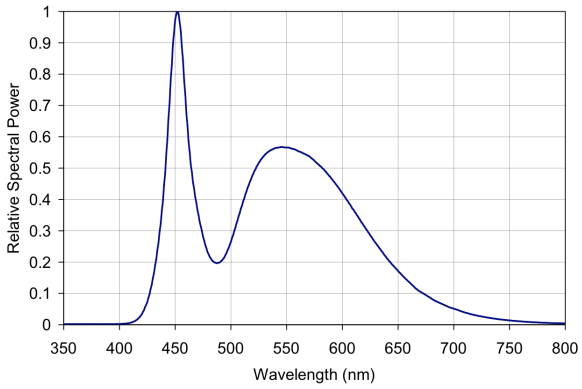

Figure 3.4: The relative spectral power of the LED Engin LZ9-00CW00 power LED. [42]

Total Harmonic Distortion

Since the LED is a non-linear component, the current is not linear with the voltage. This is shown in Figure 3.5. This means that the emitted radiation power will not be linear with the voltage as well. It is important to take this into account, since the power LEDs are powered by means of a sinusoidal voltage.

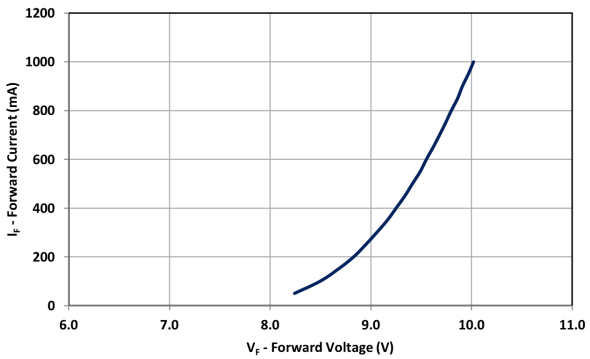

Figure 3.5: The forward current in function of the forward voltage of the LED Engin LZ9-00CW00 power LED. [42]

Therefore, a power LED was subjected to a total harmonic distortion (THD) test. In order to realize this test, a simple circuit with a photodiode and an I-V converter was built, meaning that the output voltage of the I-V converter was proportional to the emitted radiation power of the power LED. The input voltage of the power LED was a quasi-perfect sine, with a frequency of 1 Hz and a voltage ranging from 25 V to 30 V. The emitted radiation power of the power LED is shown in Figure 3.6.

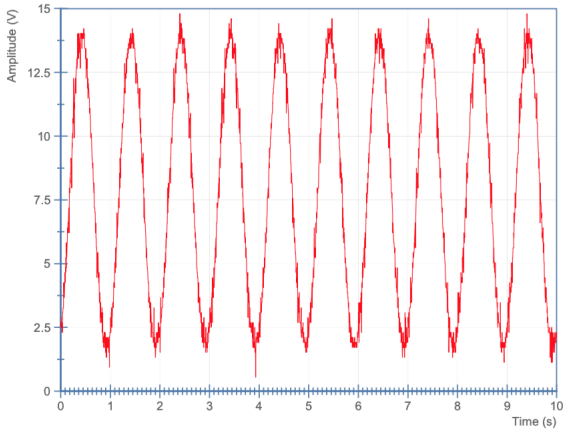

Figure 3.6: The emitted radiation power of the LED Engin LZ9-00CW00 power LED. The input signal was a sine of 1 Hz, ranging from 25 V to 30 V.

The output signal of the power LED was analyzed with a LabVIEW program and the results are summarized in Figure 3.7, in which the gain was plotted in function of the frequency. It can be noted that most of the energy is located at the fundamental frequency (1 Hz), as displayed by the peak at this frequency. From here, it is clear that only second and third harmonics are present, as displayed by the peaks at these frequencies. Note that the small peaks are caused due to noise. This noise level is dependent on the equipment, the band width, etc. The THD of the emitted radiation power from the power LED was rated at 2.35 %. Further THD tests were carried out at other frequencies, but no significant deviations were found. Therefore, it can be concluded that there is no need to take the THD into account in further calculations. [42]

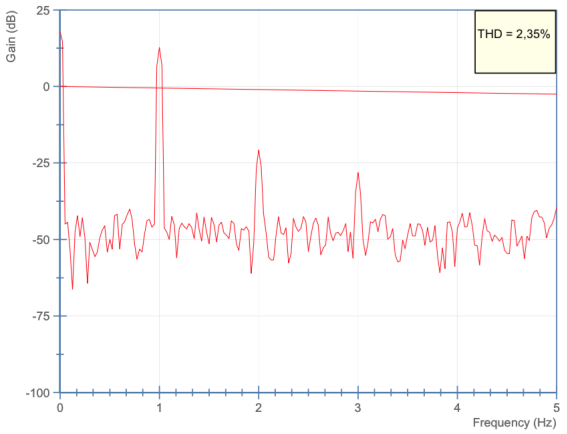

Figure 3.7: A representation of the THD of the emitted radiation power of the LED Engin LZ9-00CW00 power LED, which was rated at 2.35 %.

3.1.3 Data Analyzer

A Dell LATITUDE E5440, purchased from Dell Inc. (Round Rock, TX, USA), was used for the data acquisition and the data processing. The laptop was equipped with an Intel Core i5-4310U CPU with 8 GB DDR3 RAM. When using the FLIR A5sc IR camera, the interfacing went via an Ethernet cable, which was attached with the gigabit Ethernet port on the laptop. When using the FLIR E40 IR camera, the interfacing went via a USB cable, which was connected with the USB port on the laptop. The laptop had the software program LabVIEW installed, which makes it possible to create dedicated software in order to acquisite and process the data images. In order to analyze the test results when the processing was done, the software program ImageJ was used. The most important specifications of the data analyzer can be found in Table 3.2. [43]

Table 3.2: The specifications of the Dell LATITUDE E5440. [43]

Features	**Dell LATITUDE E5440**
Processor	Intel Core i5-4310U
Video Card	Intel HD Graphics 4400
System Type	64 Bit
RAM	8 GB DDR3
Screen Size	14” HD+ (1600x900) Anti-Glare LED-Backlit Display
Hard Drive	Up to 500 GB Solid State Hybrid Drive
Operating System	Microsoft Windows 7 Professional

3.2 Software

3.2.1 LabVIEW

The software which was used for the data acquisition and the data processing is LabVIEW, downloaded from http://www.ni.com/download-labview/. LabVIEW is a system-design platform for graphical programming designed by National Instruments. This software provides a fast and cost-efficient interface communication and is mainly used for data acquisition, instrument control and industrial automation. Although LabVIEW was originally designed for Apple Macintosh, nowadays LabVIEW also runs on other platforms such as Microsoft Windows, Linux and several versions of UNIX.

The graphical programming language which is used in LabVIEW is called 'G'. Programs created by LabVIEW are referred to as Virtual Instruments (VIs). Each VI consists of two main windows, i.e. a Front Panel and a Block Diagram, respectively shown in Figure 3.8 and Figure 3.9. These two windows are described in more detail below. The two windows are automatically generated when creating a new VI. Furthermore, comprehensive tools are included in LabVIEW. These tools are needed for analysis, display and storage of data. The several troubleshooting tools allow to debug the program code. [44–48]

3.2.1.1 The Front Panel

The Front Panel displays the graphical user interface of the VI, as shown in Figure 3.8. This Front Panel shows the data that will be processed in the Block Diagram. Only controls and indicators are placed in the Front Panel using the Controls palette, meaning that no programming takes place on the Front Panel window. Controls are the interactive inputs which provide the VI with the necessary information for the Block Diagram. The indicators are the output terminals used to display the results, based on the input parameters and the program algorithm. When both the controls and the indicators are placed on the Front Panel, they are automatically generated as nodes in the Block Diagram. [44, 47]

3.2.1.2 The Block Diagram

The Block Diagram is the graphical source code of the VI, as shown in Figure 3.9. The main purpose of the Block Diagram is to disconnect the graphical source code from the user interface. Structures and functions can be carried out using the Functions palette. Controls, indicators, functions and structures are assigned as nodes. These nodes, which are connected through wires, are objects on the Block Diagram that have inputs and/or outputs and perform operations when a VI runs.

An example of a simple VI is shown in Figure 3.8 for the user interface and Figure 3.9 for the Block Diagram. Two controls (Number 1 and Number 2) are connected with a function (Multiply) via two function inputs, while the output is connected with an indicator (Multiplier) that displays the outcome (Multiplier = Number 1 X Number 2) when the VI runs. [44, 48]

3.2.2 ImageJ

The software which is being used for the analysis of the test results is ImageJ, downloaded from http://imagej.nih.gov/ij/download.html. ImageJ is an open source, Java-based image processing program. By using ImageJ's built-in editor and a java compiler, it is possible to develop custom acquisition, analysis and processing plug-ins. Therefore, Many image analysis and processing problems can be solved using the user-written plug-ins. ImageJ is a popular platform for teaching image processing thanks to its plug-in architecture and built-in development environment. [49, 50]

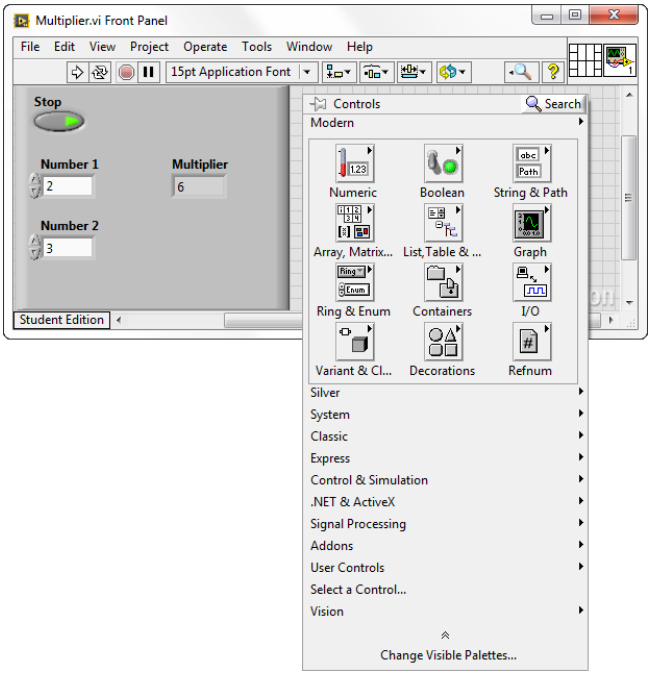

Figure 3.8: A representation of the Front Panel in LabVIEW with on the left side an example of the user interface of a simple VI and on the right side the Controls palette.

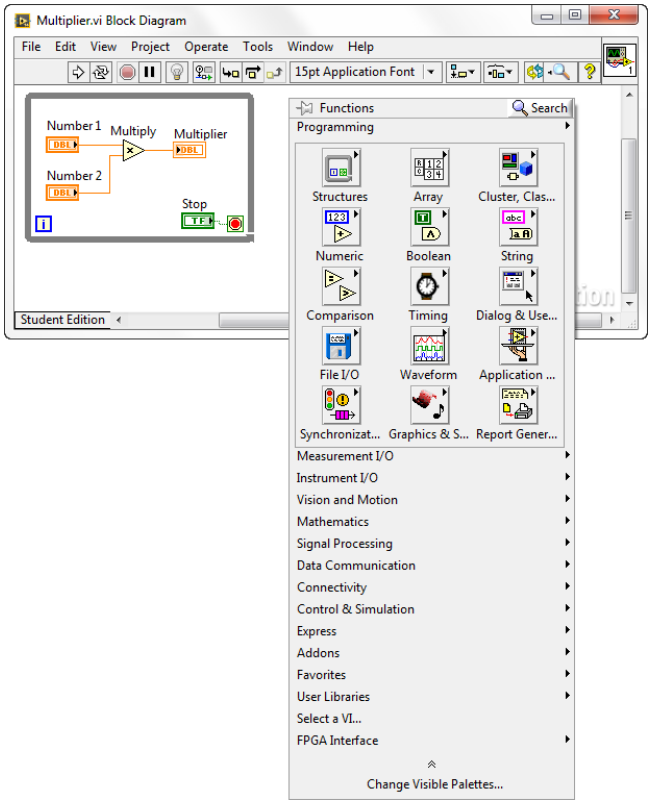

Figure 3.9: A representation of the Block Diagram in LabVIEW with on the left side an example of the graphical code of a simple VI and on the right side the Functions palette.

Chapter 4

Design Results

4.1 Hardware

4.1.1 Power Amplifier

Composition and Calculation

The Keithley 3390 Arbitrary Waveform/Function Generator was used to generate the lock-in signal for the lock-in IR thermography experiments with electrical and optical excitation. The waveform/function generator can deliver a maximum output voltage of 10 V. However, for most lock-in IR thermography experiments, a maximum output voltage up to 30 V and a maximum power output up to 100 W was needed. To solve this shortcoming, a power amplifier was built for the demo setup, as shown in Figure 4.1. This custom-made power amplifier amplifies the applied voltage 6.6 times and is able to deliver currents up to 30 A.

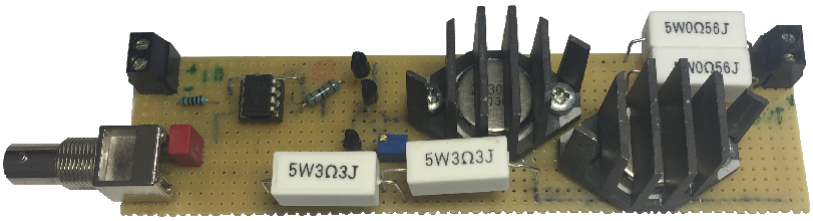

Figure 4.1: The custom-made power amplifier as used during the lock-in IR thermography experiments with electrical and optical excitation.

The following describes the calculation to obtain the above mentioned conversion. The power amplifier is constructed from a non-inverting operational amplifier (OP27), which controls two power transistors T_4 and T_5 (2N3055), powered by T_1 (BC547) and T_2 (BC337). This is represented schematically in Figure 4.2. For the calculation, it must be taken into account that each of the three transistors in series has a voltage drop of 0.7 V, which means a total voltage drop of 2.1 V at the output. Therefore, the calculations are done for an output voltage of 32.1 V. Thus, a minimum amplification factor (ζ) of 3.3 is necessary. In order to build in a reserve for other applications, a minimum ζ of 6 was desired. Equation 4.1 shows how ζ is calculated for a non-inverting operational amplifier:

$$\zeta = 1 + \frac{R_2}{R_1} \tag{4.1}$$

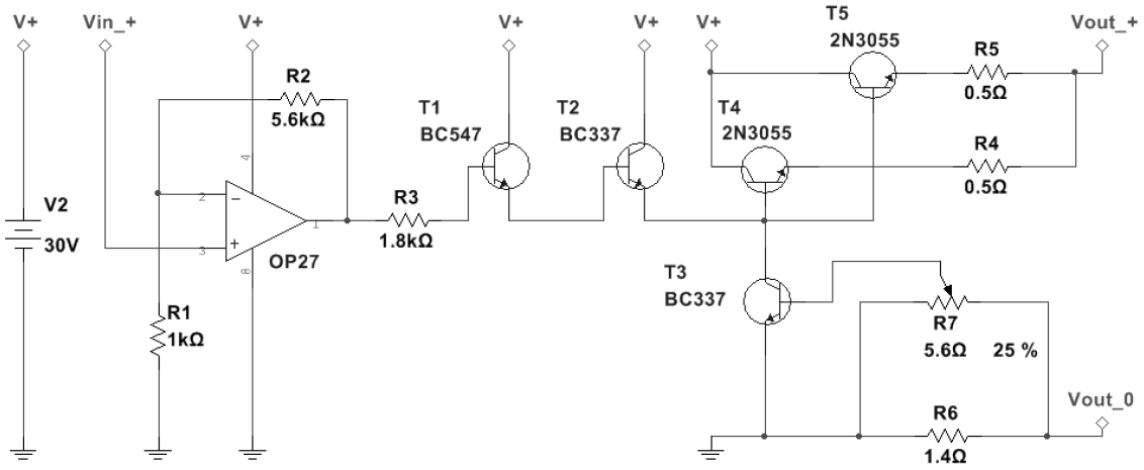

Figure 4.2: A schematic representation of the custom-made power amplifier.

From Equation 4.1, it is clear that a ζ of 6.6 can be obtained if resistor $R_1 = 1$ kΩ and resistor $R_2 = 5.6$ kΩ. Furthermore, resistor R_3 had to be calculated correctly in order to limit the output current of the operational amplifier. The value of this resistor can be calculated with Ohm's law:

$$R = \frac{U}{I} \tag{4.2}$$

Where for this case U is the maximum voltage at the output of the operational amplifier (33 V) and I is the short circuit current of the operational amplifier (20 mA). The calculated value for R_3 is 1.65 kΩ. In order to build in some reserve, resistor R_3 has a selected value of 1.8 kΩ.

Transistors T_1 and T_2 ensure a supply of sufficient electrical power in order to control the two power transistors T_4 and T_5. These power transistors each have a maximum load current of 15 A. The two resistors R_4 and R_5 are necessary to make sure both power transistors are equally loaded. Since these resistors are connected in series with the load, there will be a voltage drop across these resistors proportional to the current, as stated by Ohm's law (Equation 4.2).

Transistor T_3 (BC337) provides an overcurrent protection. This transistor goes into conduction at a base voltage starting from 0.7 V. Resistor R_6 and potentiometer R_7 are dimensioned to ensure that the base voltage of T_3 is 0.7 V whenever there is a current of 1-5 A (setting). Therefore, the replace resistance of R_6 and R_7 needs to be 0.7-0.14 Ω, as stated by Ohm's law (Equation 4.2).

Total Harmonic Distortion

Given the importance that most of the energy is located at the fundamental frequency, a THD test was carried out. The Keithley 3390 Arbitrary Waveform/Function Generator generated a sinusoidal input signal of 1 Hz, ranging from 1.5 V to 2.1 V. The output signal of the power amplifier, a sine of 1 Hz with a voltage ranging from 10 V to 14 V, was recorded with an oscilloscope. This signal is shown in Figure 4.3.

The THD of the output signal of the custom-made power amplifier was calculated with a small LabVIEW algorithm. The results are summarized in Figure 4.4, in which the gain was plotted in function of the frequency. It can be noted that most of the energy is located at the fundamental frequency of 1 Hz, as displayed by the peak at that frequency. In fact, almost no energy is found in other frequencies than the fundamental frequency. Therefore, a THD of 0.59 % was calculated by the LabVIEW algorithm. Further THD tests were carried out at other frequencies, but no significant deviations were found. Therefore, it can be concluded that there is no need to take the THD into account in further calculations.

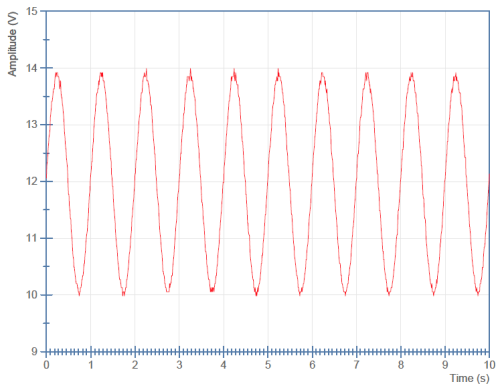

Figure 4.3: The output signal of the custom-made power amplifier. The input signal was a sine of 1 Hz, ranging from 1.5 V to 2.1 V. The output signal was a sine of 1 Hz, ranging from 10 V to 14 V.

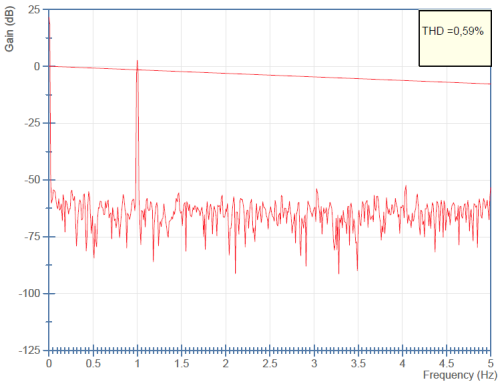

Figure 4.4: A representation of the THD of the output signal of the custom-made power amplifier, which was rated at 0.59 %.

4.2 Software

4.2.1 Lock-In Infrared Thermography in LabVIEW

In order to perform lock-in IR thermography, a program was created to capture and process the data images. What follows is a manual to operate the user interfaces of the custom-made program Lock-In Infrared Thermography, created using LabVIEW.

4.2.1.1 Main Program

When the program Lock-In Infrared Thermography is called, the user interface of the main program will be displayed, as shown in Figure 4.5. From here, it is possible to call every other subprogram necessary in order to carry out lock-in IR thermography. The different subprograms are summarized as follows:

- the Setup Function Generator subprogram allows to control the Keithley 3390 Arbitrary Waveform/Function Generator;
- the Capture Data subprogram allows to capture and save data images to a chosen directory with two possible IR cameras, i.e. the FLIR A5sc and the FLIR E40;
- the Process Data subprogram allows to process the data images from a chosen directory. Two averaging methods are provided, i.e. continuous averaging and moving averaging.

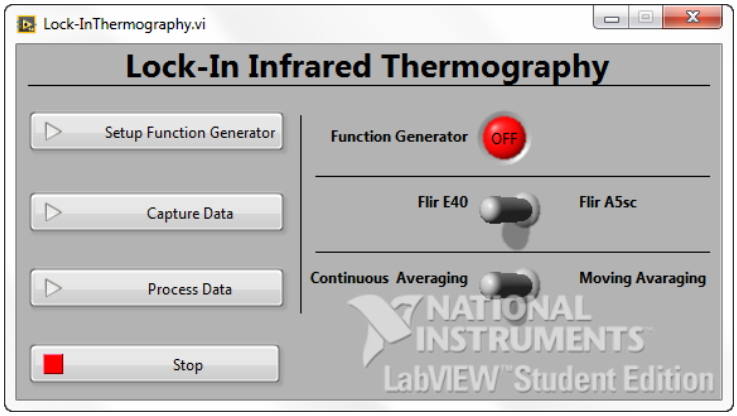

Figure 4.5: The user interface of the Lock-In Infrared Ihermography main program. From here, it is possible to call every other subprogram needed to perform lock-in IR thermography.

4.2.1.2 Setup Function Generator

When the subprogram Setup Function Generator is called from the main program, a window as shown in Figure 4.6 will be displayed. In order to setup the Keithley 3390 Arbitrary Waveform/Function Generator (discussed in Section 3.1.2), one has to set the Function Generator Name, the High Voltage, the Low Voltage, the Frequency, the Waveform and choose whether or not the function generator output should be enabled. After the setup, it is necessary to update the function generator with the Update-button. Once the function generator is set, the user can go back to the main program by clicking on the Continue-button.

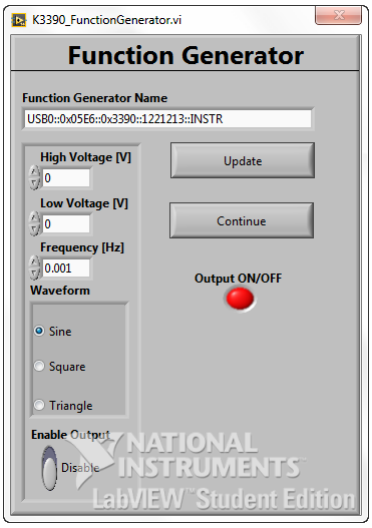

Figure 4.6: The user interface of the Setup Function Generator subprogram. With this window it is possible to control the Keithley 3390 Arbitrary Waveform/Function Generator.

4.2.1.3 Capture Data

When the subprogram Capture Data is called from the main program, a window as shown in Figure 4.7 will be displayed together with a pop-up window to choose the directory to write the captured data images to. Note that Figure 4.7 shows the window for data acquisition with the FLIR A5sc IR camera (discussed in Section 3.1.1. However, the window for data acquisition with the FLIR E40 IR camera (discussed in Section 3.1.1) is exact the same. In order to capture the data images, one has to set the Camera Name, the Lock-In Waveform and the Lock-In Frequency before clicking the Start-button. Once the program has started, the raw data images will be shown in the display at the right side of the window. The data images will automatically be saved real time in the chosen directory as portable network graphics (PNG)-files. When there is enough data captured, one can stop the acquisition by clicking the Stop-button. If the program has stopped, all meta-data, such as the camera name, the time stamp, the duration of capturing, the camera frame rate, the lock-in frequency, the lock-in waveform, the image width and the image height, will be saved in an initialize (INI)-file in the chosen path and the main program will automatically be displayed again.

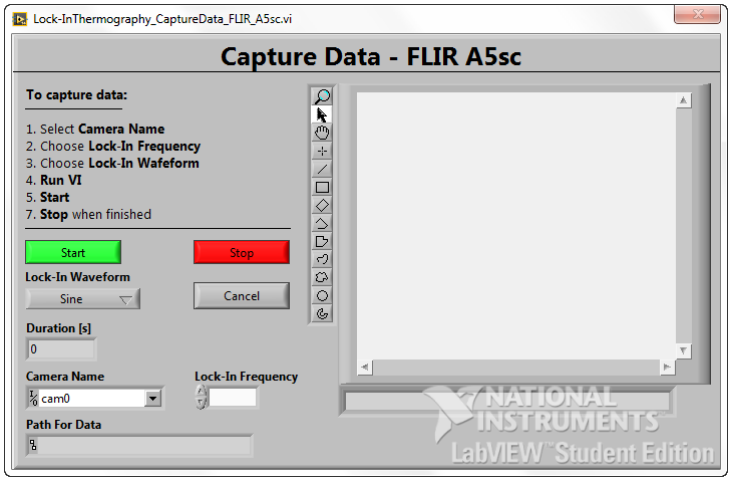

Figure 4.7: The user interface of the Capture Data subprogram for the FLIR A5sc camera. With this window it is possible to capture and save the data images to a chosen directory.

4.2.1.4 Process Data

Continuous Averaging

When the subprogram Process Data with a Continuous Averaging is called from the main program, a window as shown in Figure 4.8 will be displayed together with a pop-up window to choose the path with the raw data images to process. The chosen path includes an INI-file if the data was captured with the supplied subprogram Capture Data. The INI-file automatically sets the camera frame rate, the lock-in frequency, the lock-in waveform, the image width and the image height as was applied while capturing the raw data images. If necessary, the Lock-In Waveform and the Lock-In Frequency can be entered manually. To do so, the button Data From INI-File? must be set to NO before clicking on the Start-button. If not, the controls to enter the lock-in waveform and lock-in frequency will be greyed out. When the subprogram has started, the lock-in modulus image (at the left side) and lock-in phase image (at the right side), with a continuous averaging, will be shown in the displays at the bottom of the window. The contrast of the modulus image can be set with the Contrast Modulus-slider. The Phase image has a fixed scale, whereas the black color stands for a phase shift of -180° and the white color stand for a phase shift of +180°. However, the phase image does not provide an absolute measurement of the phase shift since it was not possible to control the phase of the function generator. Therefore, the measurement signal needs to be linked to the phase in order to be able to obtain the defect properties, such as the depth, the dimensions, etc. The program can be stopped in two ways, i.e. when all data is processed or when the user presses the Stop-button. If the program has stopped, the main program will be displayed again and the results will automatically be saved in the same directory as the raw data. However, it is also possible to save intermediate results by clicking on the Save Results-button. The outcome of this subprogram is a text (txt)-file with the pixel values of the lock-in modulus image and the lock-in phase image with a continuous averaging.

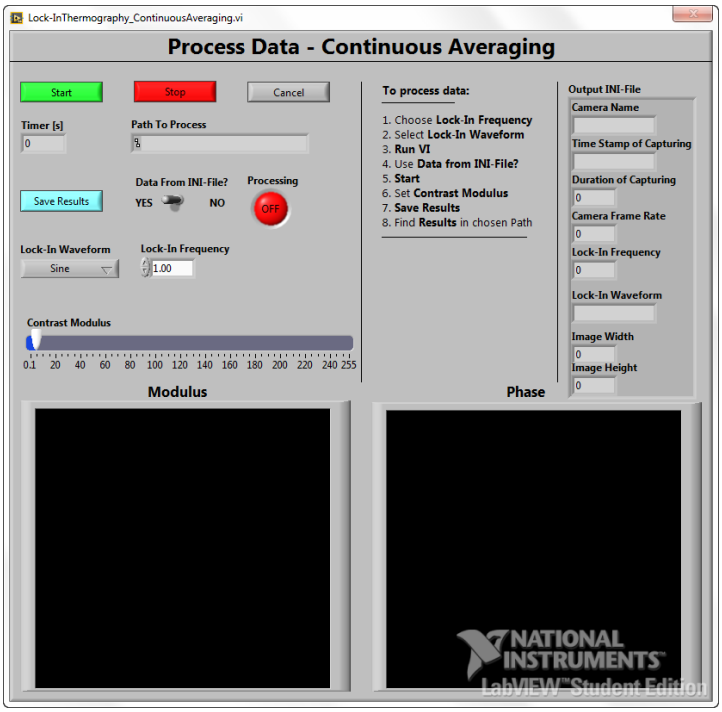

Figure 4.8: The user interface of the Process Data subprogram with a continuous averaging. From here, it is possible to process the data images with a continuous averaging from a chosen directory.

Moving Averaging

When the subprogram Process Data with a Moving Averaging is called from the main program, a window as shown in Figure 4.9 will be displayed. Basically, the operation of this subprogram is the same as Process Data with Continuous Averaging. The only difference is that, for the algorithm of a moving average, the user must specify the number of lock-in periods to average. It is important to take into account that the number of lock-in periods is a round number. When a forbidden value is entered, the program will correct this into the nearest possible value automatically. Note that the possible number of lock-in periods for averaging depends on the camera frame rate, e.g. data captured with the FLIR A5sc IR camera (frame rate of 60 Hz) can take any value as long as it is a round number (even odd numbers), whereas the value of lock-in periods has to be round and even when the data is captured with the FLIR E40 IR camera (frame rate of 7.5 Hz). When the program has started, the lock-in modulus image (at the left side) and lock-in phase image (at the right side) with a moving averaging will be shown in the displays at the bottom of the window. However, the phase image does not provide an absolute measurement of the phase shift since it was not possible to control the phase of the function generator. Therefore, the measurement signal needs to be linked to the phase in order to be able to obtain the defect properties, such as the depth, the dimensions, etc. The outcome of this subprogram is a txt-file with the pixel values of the lock-in modulus image and the lock-in phase image with a moving averaging. Since these results are only snapshots, it is interesting to manually save the results with the Save Results-button while the subprogram is processing.

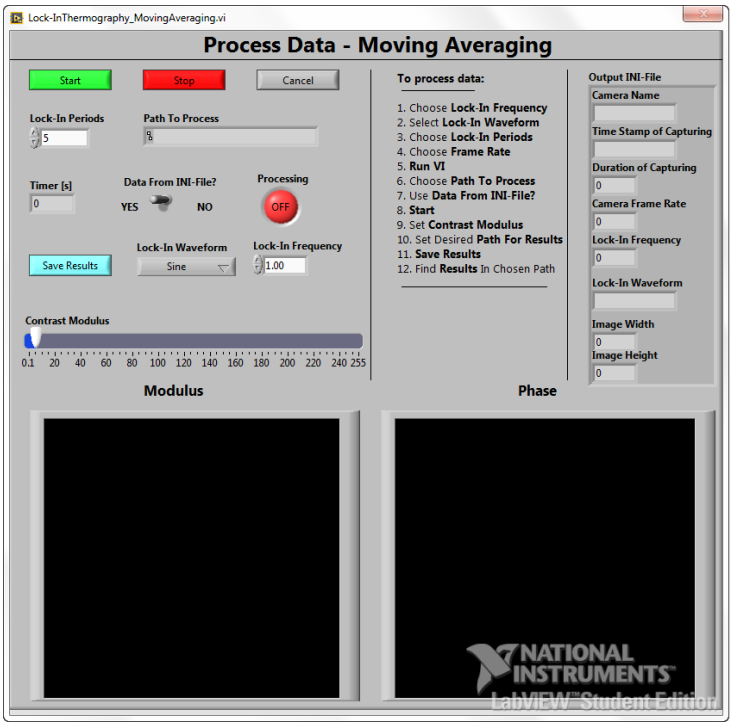

Figure 4.9: The user interface of the Process Data subprogram with a Moving Averaging. From here, it is possible to process the data images with a moving averaging from a chosen directory.

Chapter 5

Defect Detection using Lock-In Infrared Thermography

5.1 Photovoltaic Cell

5.1.1 Introduction

Due to the current environmental concerns, the number of photovoltaic (PV) plants has experienced a strong growth in the past decade. In order to obtain as much energy as possible from those plants, it is desirable that each PV module operates as close as possible to its maximum power point. To achieve this, it is necessary that all individual PV cells of the entire PV module are operational without defects, such as fractures, delaminations, hot spots, etc. Most of the time, these defects are neither visible by the naked eye nor by an IR image using passive IR thermography. Therefore, a test setup was constructed to test PV cells for their operation. This lock-in IR thermography experiment was conducted on a Conrad YH-26X46 PV cell, which was able to generate a voltage up to 0.5 V and a current up to 100 mA. [51]

5.1.2 Experimental Setup

The schematic setup to subject a PV cell to a lock-in IR thermography experiment with electrical excitation is shown in Figure 5.1.

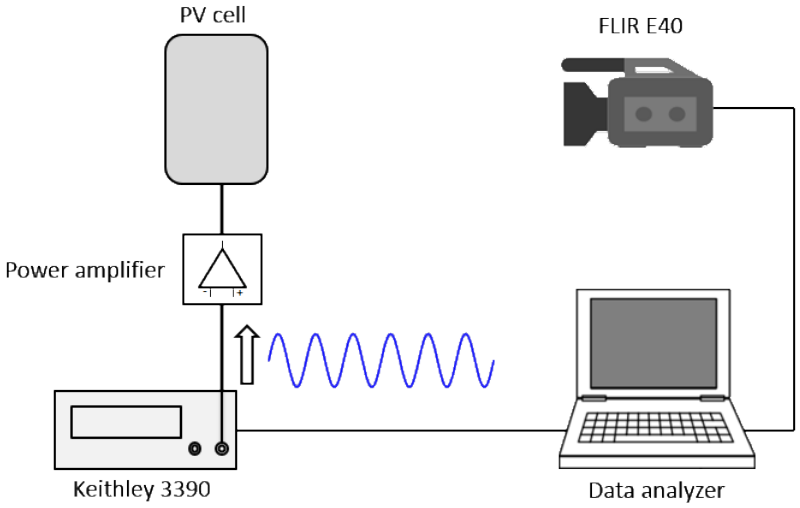

Figure 5.1: The experimental setup in order to subject a PV cell to a lock-in IR thermography experiment with electrical excitation.

The electrical excitation signal, which was generated by the Keithley 3390 Arbitrary Waveform/ Function Generator, was a sinusoidal voltage of 1 Hz, ranging from 0.8 V to 5 V. This signal was amplified by the custom-made power amplifier with an amplification factor of 6.6, resulting in a sinusoidal voltage with a frequency of 1 Hz, ranging from 8 V to 30 V. When this signal was applied to the PV cell, it caused a sinusoidal current to flow, ranging from 0.25 A to 1 A. The FLIR E40 IR camera was used to observe the PV cell during 130 s. It was mounted in front of the PV cell at a distance of 0.4 m, the frame rate was 7.5 Hz and the resolution was 320 x 245 pixels.

5.1.3 Test Results

During the 130 s lasting lock-in IR thermography experiment, the FLIR E40 IR camera provided a stream of 970 IR images, of which one image is displayed in Figure 5.2.

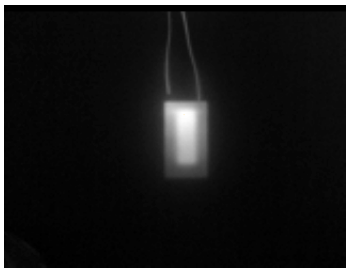

Figure 5.2: An element of the IR image stream of the PV cell, as provided by the FLIR E40 IR camera.

The provided IR images were processed with the Lock-In Infrared Thermography program with a continuous averaging (discussed in Section 2.3.3). The reference signal was a sinusoidal lock-in signal of 1 Hz. The modulus and phase image are respectively displayed in Figure 5.3 and Figure 5.4. It is clear that the thermal conductivity is not the same throughout the entire PV cell, as can be concluded from the black areas in the provided lock-in images. The black area is a strong indication of a subsurface defect or a subsurface component with a high thermal inertia. In order to exclude that the black area was not caused by a subsurface defect, this experiment was performed again with an identical PV cell. No significant differences were observed compared to the first experiment, indicating that the PV cell did not contain an internal defect.

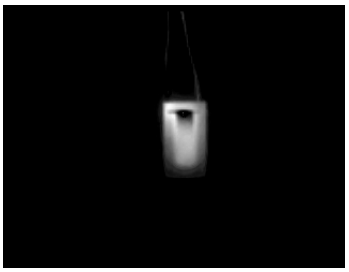

Figure 5.3: The modulus image of the PV cell subjected to a lock-in IR thermography experiment.

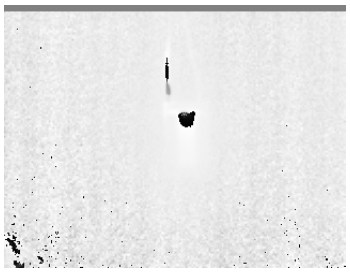

Figure 5.4: The phase image of the PV cell subjected to a lock-in IR thermography experiment.

5.1.4 Conclusion

While the IR image stream appeared to be normal, an inhomogeneity was observed by the lock-in IR thermography experiment. The black area on the lock-in images of the PV cell is caused due to a component with a high thermal inertia. The phase image was only relatively correct. Therefore, it was not possible to obtain more information about the black area, such as the depth, etc.

5.2 Meander Resistor

5.2.1 Introduction

A meander resistor can be considered as a bar resistor with the exception of the corner squares (right-angle bends). Additionally, the tracks of the meander resistor are often located at micrometer distance of each other. Therefore, a short circuit between two adjacent tracks is not unlikely. Of course, this affects a proper operation of the meander resistor. Most of the time, a short circuit between two adjacent tracks is neither visible by the naked eye nor by an IR image using passive IR thermography. Therefore, a test setup was constructed to test meander resistors for their operation. This lock-in IR thermography experiment was conducted on a custom-made meander resistor, which had a total resistance of 20 Ω. Note that a power resistor of 80 Ω was connected in series with the meander resistor to limit the current. [52]

5.2.2 Experimental Setup

The schematic setup to subject a meander resistor to a lock-in IR thermography experiment with electrical excitation is shown in Figure 5.5.

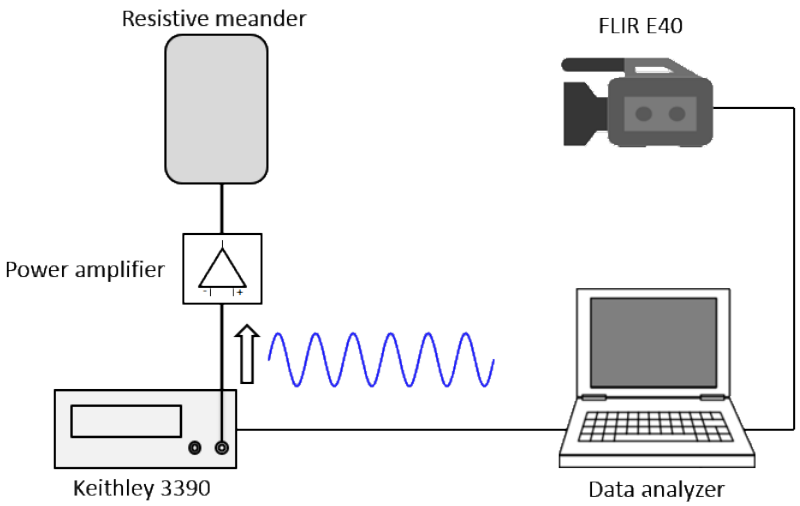

Figure 5.5: The experimental setup in order to subject a meander resistor to a lock-in IR thermography experiment with electrical excitation.

The electrical excitation signal, which was generated by the Keithley 3390 Arbitrary Waveform/ Function Generator, was a sinusoidal voltage of 1 Hz, ranging from 0.8 V to 5 V. This signal was amplified by the power amplifier with an amplification factor of 6.6, resulting in a sinusoidal voltage with a frequency of 1 Hz, ranging from 8 V to 30 V. When this signal was applied to the series circuit, it caused a sinusoidal current to flow, ranging from 0.08 A to 0.3 A. The voltage across the meander resistor had a value ranging from 1.6 V to 6 V. The FLIR E40 IR camera was used to observe the meander resistor during 130 s.. It was mounted in front of the meander resistor at a distance of 0.4 m, the frame rate was 7.5 Hz and the resolution was 320 x 245 pixels.

5.2.3 Test Results

During the 130 s lasting lock-in IR thermography experiment, the FLIR E40 IR camera provided a stream of 970 IR images, of which one image is displayed in Figure 5.6.

Figure 5.6: An element of the IR image stream of the meander resistor, as provided by the FLIR E40 IR camera.

The provided IR images were processed with the Lock-In Infrared Thermography program with a continuous averaging (discussed in Section 2.3.3). The reference signal was a sinusoidal lock-in signal of 1 Hz. The modulus and phase image are respectively displayed in Figure 5.7 and Figure 5.8. Note that these lock-in images only provide information about the components with a thermal signal which is fluctuating at the lock-in frequency. This is represented in this test by two phenomena:

1. the power resistor, which is clearly visible in the IR image stream, has disappeared from the lock-in images due to a big thermal inertia;
2. the hand, which is slightly visible in the IR image stream, has disappeared from the lock-in images because its thermal radiation is constant.

Note that the modulus image includes a moiré pattern, which is caused due to the small distance between the tracks and the limited resolution of the IR camera. Due to this phenomenon, it is not possible to make a conclusive judgment about the functioning of the meander resistor.

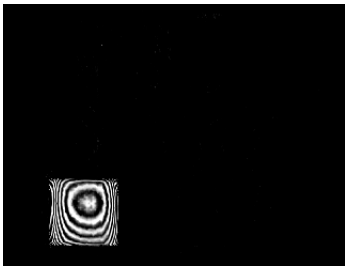

Figure 5.7: The modulus image of the meander resistor subjected to a lock-in IR thermography experiment.

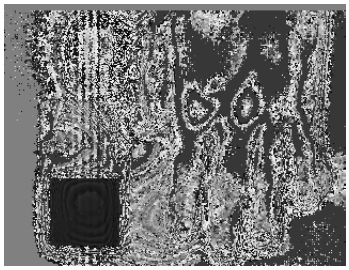

Figure 5.8: The phase image of the meander resistor subjected to a lock-in IR thermography experiment.

5.2.4 Conclusion

This experiment displayed the major advantage of lock-in IR thermography: the lock-in images only provide information about the components with a thermal signal which is fluctuating at the lock-in frequency. Due to the moiré pattern, it was not possible to make a conclusive judgment about the functioning of the meander resistor. A more sensitive IR camera will provide a solution for this problem.

5.3 Carbon Fiber Reinforced Polymer Substrate

5.3.1 Introduction

Carbon fiber reinforced polymer (CFRP) is a polymer matrix composite material reinforced by carbon fibers. CFRP provides a high modulus of elasticity, a high tensile strength, a low density, etc. Therefore, it is a commonly used material where a high tensile strength combined with a low density is required. These two features combined gives an increased chance of defects, such as inhomogeneities, delaminations and internal fractures, which indicate a reduction of the tensile strength. Most of the time, these defects are neither visible by the naked eye nor by an IR image using passive IR thermography. Therefore, a test setup was constructed to test CFRP substrates for their characteristics. This lock-in IR thermography experiment was conducted on a CFRP tube, which had an internal diameter of 18 mm and an external diameter of 20 mm. In this section, two lock-in IR thermography experiments were conducted:

1. the characterization of the CFRP tube without defects;
2. the characterization of the CFRP tube with defects. [53]

5.3.2 Experimental Setup

The schematic setup to subject a CFRP substrate to a lock-in IR thermography experiment with electrical excitation is shown in Figure 5.9.

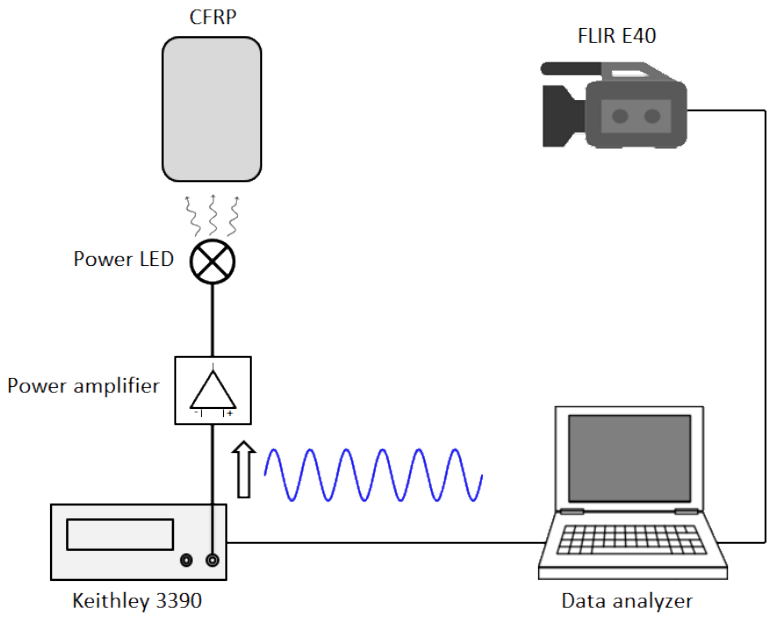

Figure 5.9: The experimental setup in order to subject a CFRP substrate to a lock-in IR thermography experiment with optical excitation.

The optical excitation signal, which was generated by four LED Engin LZ9-00CW00 power LEDs, was a sinusoidal electromagnetic signal of 0.5 Hz, ranging from 0 W to 80 W. The electrical signal of the power LEDs was generated by the Keithley 3390 Arbitrary Waveform/Function Generator, a sinusoidal voltage of 0.5 Hz, ranging from 3.8 V to 5 V. This signal was amplified by the power amplifier with an amplification factor of 6.6, resulting in a sinusoidal voltage with a frequency of 0.5 Hz, ranging from 25 V to 30 V. The FLIR E40 IR camera was used to observe the CFRP substrate during 1000 s. It was mounted in front of the CFRP substrate at a distance of 0.4 m, the frame rate was 7.5 Hz and the resolution was 320 x 245 pixels.

5.3.3 Test Results without Defect

During the first 1000 s lasting lock-in IR thermography experiment, the FLIR E40 IR camera provided a stream of 7500 IR images, of which one image is displayed in Figure 5.10.

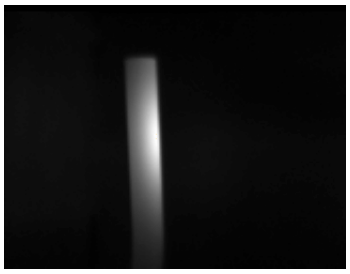

Figure 5.10: An element of the IR image stream of the CFRP substrate without defect, as provided by the FLIR E40 IR camera.

The provided IR images were processed with the Lock-In Infrared Thermography program with a continuous averaging (discussed in Section 2.3.3). The reference signal was a sinusoidal lock-in signal of 0.5 Hz. The modulus and phase image are respectively displayed in Figure 5.11 and Figure 5.12. From these images, it is clear that the thermal conductivity is the same throughout the entire CFRP substrate. Note that the substrate was optically excited from the right side, as can be seen by the high intensity at that side in Figure 5.10. This caused a small disturbance in the lock-in images since the heat of the LEDs (with a high thermal inertia) reflected on the substrate.

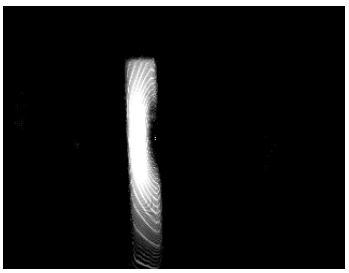

Figure 5.11: The phase image of the CFRP substrate without defect subjected to a lock-in IR thermography experiment.

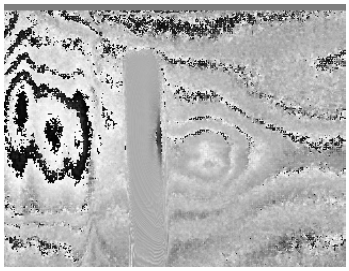

Figure 5.12: The phase image of the CFRP substrate without defect subjected to a lock-in IR thermography experiment.

5.3.4 Test Results with Defect

During the second 1000 s lasting lock-in IR thermography experiment, the FLIR E40 IR camera provided a stream of 7500 IR images, of which one image is displayed in Figure 5.13.

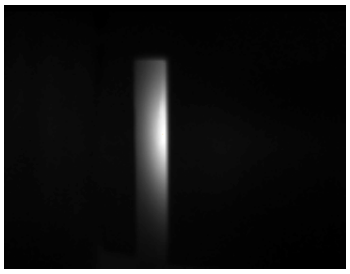

Figure 5.13: An element of the IR image stream of the CFRP substrate with defect, as provided by the FLIR E40 IR camera.

The provided IR images were processed with the Lock-In Infrared Thermography program with a continuous averaging (discussed in Section 2.3.3). The reference signal was a sinusoidal lock-in signal of 0.5 Hz. The modulus and phase image are respectively displayed in Figure 5.14 and Figure 5.15. While the IR image stream (Figure 5.13) appeared to be normal, it is clear that the thermal conductivity is not the same throughout the entire CFRP substrate. Therefore, it can be concluded an internal fracture is located at the dark area in the modulus image. However, since the phase image is only relatively correct, it is not possible to obtain more information about the defected area, such as the defect depth, etc.

Figure 5.14: The modulus image of the CFRP substrate with defect subjected to a lock-in IR thermography experiment.

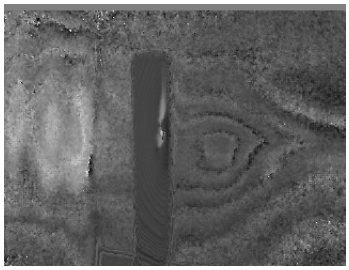

Figure 5.15: The phase image of the CFRP substrate with defect subjected to a lock-in IR thermography experiment.

5.3.5 Conclusion

The first experiment displayed a defect-free CFRP substrate, as can be concluded from the normal temperature profile in the modulus image. The second experiment displayed an internal fracture in the CFRP substrate, while the IR image stream appeared to be normal. However, only the defect dimensions can be indicated since the phase image was only relatively correct. Nevertheless, it is appropriate to replace the defected CFRP substrate.

Chapter 6

Conclusions

IR thermography is one of the many techniques used for NDT of various materials and is a useful tool to determine subsurface defects that are not visible for the naked eye. NDT is preferred over destructive testing since characterization tests can be performed without damaging the material. Lock-in IR thermography is a specific type of NDT. The principle of lock-in IR thermography is based on the excitation of a periodic thermal signal on the the material under test, as discussed in Section 2.3.

During this master's thesis, a demo setup to perform lock-in IR thermography was developed. Both hardware and software for this demo setup are discussed within this dissertation. Every hardware component is explained in detail. For the software, the user interfaces are explained. THD tests were carried out on the power amplifier and power LED. Additionally, several defect detection tests were carried out, including the characterization of a PV cell, a meander resistor and a CFRP substrate.

The hardware, discussed in Section 3.1, consists of (i) an IR camera (the FLIR E40 or the FLIR A5sc IR camera), (ii) an excitation source (the function generator or the power LEDs) and (iii) a data analyzer. During the defect detection tests, the FLIR E40 IR camera was primarily used because the parameters of the FLIR A5sc IR camera did alter during the experiments. As a consequence, the data was no longer accurate. Both IR cameras had their advantages and disadvantages, which should be carefully considered when deciding which IR camera to use during an experiment. The available function generator (the Keithley 3390 Arbitrary Waveform/Function Generator) was not capable of generating enough power to excite a thermal signal. In order to cope with this problem, a custom-made power amplifier was constructed, which is discussed in Section 4.1.

A multifunctional software program was created using LabVIEW, as discussed in Section 3.2. With this program (i) the function generator was controlled, (ii) IR data images were captured and stored and (iii) IR data images were processed to generate a modulus and phase image. If desired, the software can be obtained by contacting prof. dr. ir. Michaël Daenen: michael.daenen@uhasselt.be.

Two THD tests were carried out. The first THD test was conducted on the output signal of the custom-made power amplifier and is discussed in Section 4.1.1. The results showed that the THD of this signal was relatively low (0.59 %). The second THD test was carried out on the emitted radiation power of the power LEDs and is discussed in Section 3.1.2. The results demonstrated that 2.35 % of the total radiated power was distributed between other frequencies different from the fundamental frequency.

Three defect detection tests were carried out using the demo setup. First, a PV cell was subjected to a lock-in IR thermography experiment with electrical excitation, discussed in Section 5.1. This experiment indicated that a component with a high thermal inertia was located underneath the surface. Second, a meander resistor was subjected to a lock-in IR thermography experiment with electrical excitation, discussed in Section 5.2.. No conclusive judgment about the functioning of the meander resistor could be provided because the resolution of the IR camera was insufficient to distinguish adjacent tracks. This resulted in a moiré pattern, which was visible on the modulus image. Third, a CFRP specimen was subjected to a lock-in IR thermography experiment with optical excitation, discussed in Section 5.3.. The results showed no defects. After an impact on the CFRP substrate was simulated, the lock-in images showed an internal fracture.

After this master's thesis, it can be concluded that the demo setup for lock-in IR thermography can detect subsurface defects. However, the phase image does not provide an absolute measurement of the phase shift since it was not possible to control the phase of the function generator. Therefore, the measurement signal needs to be linked to the phase in order to be able to obtain the defect properties, such as the depth, the dimensions, etc.

Bibliography

[1] University Hasselt, "IMO - IMOMEC," Accessed February 20th 2015. [Online]. Available: http://www.uhasselt.be/IMO

[2] M. Vollmer and K.-P. Möllmann, *Infrared Thermal Imaging: Fundamentals, Research and Applications*. John Wiley & Sons, 2011.

[3] E. Wieërs and S. Wouters, *Fysica voor Industrieel Ingenieurs Deel 1*. Pearson, 2011.

[4] NASA, "Electromagnetic Spectrum Diagram," Accessed April 7th 2015. [Online]. Available: http://mynasadata.larc.nasa.gov/science-processes/electromagnetic-diagram/

[5] T. West, *The Ultimate Infrared Handbook for R & D Professionals*. FLIR systems Inc., 2012.

[6] NASA, "Infrared Waves," Accessed April 7th 2015. [Online]. Available: http://science.hq.nasa.gov/kids/imagers/ems/infrared.html

[7] P. Michaud, "What is Infrared Radiation?" Accessed April 7th 2015. [Online]. Available: http://www.gemini.edu/public/infrared.html

[8] Centre for Remote Imaging Sensing and Processing, "Principles of Remote Sensing," Accessed April 7th 2015. [Online]. Available: http://www.crisp.nus.edu.sg/~research/tutorial/em.htm

[9] W. Herschel, "Experiments on the refrangibility of the invisible rays of the sun," *Philosophical Transactions of the Royal Society of London*, vol. 90, pp. 284–292, 1800.

[10] Cool Cosmos, "Herschel Discovers Infrared Light," Accessed April 7th 2015. [Online]. Available: http://coolcosmos.ipac.caltech.edu/cosmic_classroom/classroom_activities/herschel_bio.html

[11] E. Britannica, "Planck's Radiation Law," Accessed April 7th 2015. [Online]. Available: http://www.britannica.com/EBchecked/topic/462936/Plancks-radiation-law

[12] O. Breitenstein, W. Warta, and M. Langenkamp, *Lock-in Thermography*, ser. Springer Series in Advanced Microelectronics. Berlin, Heidelberg: Springer, 2010, vol. 10.

[13] R. Usamentiaga, P. Venegas, J. Guerediaga, L. Vega, J. Molleda, and F. G. Bulnes, "Infrared thermography for temperature measurement and non-destructive testing." *Sensors (Basel, Switzerland)*, vol. 14, no. 7, pp. 12 305–48, Jan. 2014.

[14] X. Maldague, "Introduction to NDT by active infrared thermography," *Materials Evaluation*, pp. 1–22, 2002.

[15] US Department of Commerce, "ESRL Global Monitoring Division - Global Greenhouse Gas Reference Network," Accessed April 7th 2015. [Online]. Available: http://www.esrl.noaa.gov/gmd/ccgg/trends/

[16] Wikipedia, "Atmosfaerisk Spredning," Accessed April 7th 2015. [Online]. Available: http://commons.wikimedia.org/wiki/File:Atmosfaerisk_spredning.png

[17] J. S. Byrnes, *Unexploded Ordnance Detection and Mitigation.* Springer, 2009.

[18] D. Bursell, "Selecting an IR Detector for Thermographic Imaging," Accessed April 8th 2015. [Online]. Available: http://www.rdmag.com/articles/2007/12/selecting-ir-detector-thermographic-imaging

[19] O. Inc., "Thermal Imaging Camera - Microbolometer Detectors," Accessed April 9th 2015. [Online]. Available: http://www.optotherm.com/microbolometers.htm

[20] R. Kumar, B. Karunagaran, D. Mangalaraj, S. Narayandass, P. Manoravi, M. Joseph, V. Gopal, R. Madaria, and J. Singh, "Room Temperature Deposited Vanadium Oxide Thin Films for Uncooled Infrared Detectors," *Materials Research Bulletin*, vol. 38, no. 7, pp. 1235–1240, Jun. 2003.

[21] K. K. Deb, "Protein-Based Thin Films: A New High-TCR Material," pp. 52–55, 2000.

[22] A. Manohar, "Quantitative Nondestructive Testing using Infrared Thermography," Jan. 2012.

[23] Thermografisch Adviesbureau BV, "Advantages of Thermography," Accessed April 9th 2015. [Online]. Available: http://www.thermography.nl/index.php/advantages

[24] F. Colbert, "Understanding Prorietary Infrared Image Files," Accessed April 9th 2015. [Online]. Available: http://www.irinfo.org/articleofmonth/pdf/article_4_2006_colbert.pdf

[25] Z.-H. Chen, T. Uchida, and S. Minami, "Real-Time Emissivity Corrected Infrared Microthermography Based on a Double Modulation Technique," *Measurement Science and Technology*, vol. 4, no. 3, pp. 288–292, Mar. 1993.

[26] J. Snell and J. Renowden, "Improving Results of Thermographic Inspections of Electrical Transmission and Distribution Lines," pp. 135–144, 2000.

[27] L. Cartz, *Nondestructive Testing: Radiography, Ultrasonics, Liquid Penetrant, Magnetic Particle, Eddy Current.* ASM International, 1995.

[28] O. Breitenstein and J. Rakotoniaina, "New developments in IR lock-in thermography," 2004.

[29] J. Bauer, O. Breitenstein, and J. Wagner, "Lock-in thermography: a versatile tool for failure analysis of solar cells," *. . . Device Failure Analysis*, pp. 6–12, 2009.

[30] M. Zimnoch, W. Oliferuk, and M. Maj, "Estimation of Defect Depth in Steel Plate using Lock-In IR Thermography," *Acta Mechanica et Automatica*, vol. Vol. 4, no. 4, pp. 106–109, 2010.

[31] G. M. Carlomagno and C. Meola, "Comparison Between Thermographic Techniques for Frescoes NDT," *NDT & E International*, vol. 35, no. 8, pp. 559–565, Dec. 2002.

[32] S. W. Smith, *The Scientist and Engineer's Guide to Digital Signal Processing.* California Technical Pub., 1997.

[33] I.-C. Clemente, G. Marc, P. Jean-Marc, S. Guibert, A. Bendada, and X. P. V. Maldague, "Active Infrared Thermography Techniques for the Nondestructive Testing of Materials," pp. 1–25, Nov. 2014.

[34] N. P. Avdelidis, T.-H. Gan, C. Ibarra-Castanedo, and X. P. V. Maldague, "Infrared Thermography as a Non-Destructive Tool for Materials Characterisation and Assessment," pp. 801 313–801 313–7, May 2011.

[35] M. Tarin and R. Rotolante, "NDT in Composite Materials with Flash , Transient , and Lock-in Thermography," pp. 1–4, 2010.

[36] FLIR Systems Inc., "FLIR A5sc, A15sc, & A35sc Camera Kits," Accessed April 28th 2015. [Online]. Available: http://www.flir.com/thermography/americas/ca/fr/view/?id=58197&collectionid=686&col=58200

[37] FLIR Systems Inc., "FLIR Série E," Accessed April 28th 2015. [Online]. Available: http://www.flir.fr/cs/display/?id=41372

[38] FLIR Systems Inc., "Datasheet FLIR E-Series," 2013.

[39] FLIR Systems Inc., "Thermal Imaging Camera Bench Test Thermal Kits," 2014.

[40] Keithley Instruments Inc., "Model 3390 Arbitrary Waveform Generator User's Manual," January 2009.

[41] Keithley Instruments Inc., "3390 Arbitrary Function Generator/Waveform Generators," Accessed Oktober 20th 2015. [Online]. Available: http://www.keithley.com/products/dcac/waveform/arb/?mn=3390

[42] Led Engin Inc., "Datasheet LZ9-00CW00," 2014.

[43] Dell Inc., "Lattitude E5440," Accessed May 21th 2015. [Online]. Available: http://www.dell.com/us/business/p/latitude-e5440-laptop/pd

[44] Wikipedia, "LabVIEW," Accessed April 10th 2015. [Online]. Available: http://en.wikipedia.org/wiki/LabVIEW

[45] National Instruments, "LabVIEW," Accessed April 10th 2015. [Online]. Available: http://belgium.ni.com/labview

[46] Wikipedia, "Macintosh Classic," Accessed April 10th 2015. [Online]. Available: http://en.wikipedia.org/wiki/Macintosh_Classic

[47] National Instruments, "Tutorial: Front Panel," Accessed April 10th 2015. [Online]. Available: http://www.ni.com/white-paper/7566/en/

[48] National Instruments, "Tutorial: Block Diagram," Accessed April 10th 2015. [Online]. Available: http://www.ni.com/tutorial/7565/en/

[49] ImageJ, "ImageJ," Accessed May 25th 2015. [Online]. Available: http://imagej.net/Welcome

[50] Wikipedia, "ImageJ," Accessed May 25th 2015. [Online]. Available: http://en.wikipedia.org/wiki/ImageJ

[51] Conrad Electronic SE, "Datasheet Conrad YH-26X46 PV Cell," 2008.

[52] O. Tesson and F. Barbier, "Meander resistor," Oct. 6 2011, US Patent App. 13/002,082. [Online]. Available: http://www.google.com/patents/US20110241820

[53] D. Kopeliovich, "Carbon Fiber Reinforced Polymer Composites," Accessed May 28th 2015. [Online]. Available: http://www.substech.com/dokuwiki/doku.php?id=carbon_fiber_reinforced_polymer_composites

Auteursrechtelijke overeenkomst

Ik/wij verlenen het wereldwijde auteursrecht voor de ingediende eindverhandeling:
Lock-in infrared thermography as non-destructive test for material characterization

Richting: **master in de industriële wetenschappen: energie-elektrotechniek**
Jaar: **2015**

in alle mogelijke mediaformaten, - bestaande en in de toekomst te ontwikkelen - , aan de Universiteit Hasselt.

Niet tegenstaand deze toekenning van het auteursrecht aan de Universiteit Hasselt behoud ik als auteur het recht om de eindverhandeling, - in zijn geheel of gedeeltelijk -, vrij te reproduceren, (her)publiceren of distribueren zonder de toelating te moeten verkrijgen van de Universiteit Hasselt.

Ik bevestig dat de eindverhandeling mijn origineel werk is, en dat ik het recht heb om de rechten te verlenen die in deze overeenkomst worden beschreven. Ik verklaar tevens dat de eindverhandeling, naar mijn weten, het auteursrecht van anderen niet overtreedt.

Ik verklaar tevens dat ik voor het materiaal in de eindverhandeling dat beschermd wordt door het auteursrecht, de nodige toelatingen heb verkregen zodat ik deze ook aan de Universiteit Hasselt kan overdragen en dat dit duidelijk in de tekst en inhoud van de eindverhandeling werd genotificeerd.

Universiteit Hasselt zal mij als auteur(s) van de eindverhandeling identificeren en zal geen wijzigingen aanbrengen aan de eindverhandeling, uitgezonderd deze toegelaten door deze overeenkomst.

Voor akkoord,

Bussé, Len **Carolus, Jorne**

Datum: **31/05/2015**